



# Efficient and energy stable scheme for the hydrodynamically coupled three components Cahn-Hilliard phase-field model using the stabilized-Invariant Energy Quadratzation (S-IEQ) Approach

Xiaofeng Yang

Department of Mathematics, University of South Carolina, Columbia, SC 29208, USA



## ARTICLE INFO

### Article history:

Available online 20 April 2021

### Keywords:

Second-order  
Phase-field  
Cahn-Hilliard  
Three-phase  
Unconditional energy stability  
Stabilized-IEQ

## ABSTRACT

In this paper, we consider numerical approximations for solving the hydrodynamically coupled three components Cahn-Hilliard phase-field model. By combining the Invariant Energy Quadratzation approach with the stabilization technique, and the projection method for the Navier-Stokes equations, we obtain a linear, second-order, and unconditionally energy stable time marching scheme. We present rigorous proofs for the well-posedness of the obtained linear system and the unconditional energy stability. Various 2D and 3D numerical simulations are implemented to demonstrate the stability and accuracy of the scheme thereafter.

© 2021 Elsevier Inc. All rights reserved.

## 1. Introduction

In this paper, we consider numerical approximations for solving the hydrodynamically coupled three components Cahn-Hilliard phase-field model that was developed in [4–6]. As one of the most popular modeling approaches for interfacial dynamics, the phase-field method had been widely applied in simulating a variety of multiple-component material, e.g., multiphase fluid flows, vesicle membranes, crystals, fracture dynamics, etc., see [6,9,11,16,17,31,42] and the references therein. The governing equations in phase-field models are derived from the energy-based variational formalism and thus the system obeys the so-called energy dissipation law. For instance, the commonly-used total free energy for simulating the two-phasic material system usually includes two parts where one is the bulk potential (double-well or logarithmic Flory-Huggins) that yields a hydrophobic contribution, and the other one is the conformational capillary entropic term that demands a hydrophilic property. The competition between these two types of energy potentials enforces the coexistence of two distinct phases in the immiscible two-phasic system. Concerning the theoretical analysis, algorithm developments and numerical simulations of the two-phasic system in simulating various materials, we refer to [9–12,15,17,19,22–24,28].

Similar to the two-phasic scenario, the essential idea to model the three components material system is to adopt three independent phase-field variables to represent the volume (or mass) fraction of each component and then impose a hyperplane link condition (i.e., no volume leaking) for them (see [1–4,6,9,13,14,18–20,26]). The free energy of the system naturally turns out to be the summation of the original biphasic energy that appeared in the two-phasic model for each variable. Moreover, a Lagrangian multiplier is adopted in each Cahn-Hilliard equation to enforce the hyperplane link condition. But such a simple system is not well-posed for the *total spreading* case and some nonphysical instabilities at interfaces

E-mail address: [xfyang@math.sc.edu](mailto:xfyang@math.sc.edu).

may occur, which was illustrated in [4,6]. To fix this issue, in [4,6], a sixth-order polynomial type coupling potential is added into the free energy that can ensure the system to be well-posed. However, since the three phase-field variables are completely coupled together by this term, numerical difficulties to design efficient and energy stable schemes are increased to a large extent. Remarkably, most of the existing methods are either first-order accurate in time, or energy unstable, or highly nonlinear, or even the combinations of these features (see [4,6,25]) except the most recently developed so-called Invariant Energy Quadratization (IEQ) [43] and Scalar Auxiliary Variable (SAV) [45,46] approaches that could generate some second-order accurate schemes with unconditional energy stability.

Meanwhile, we note almost all the above-mentioned numerical algorithms were focused on the partial model instead of the full hydrodynamically coupled model while the three-phase model had been given attention for more than a decade. Remarkably, the full model is conceivably more complicated for algorithm developments than the partial model since it includes more nonlinear coupling terms between the flow field and the phase-field variable except the stiffness issue induced by the thin interfacial parameter and the sixth-order polynomial term. For the full model, to the best of the author's knowledge, the only scheme with unconditional energy stability for arbitrary time steps is developed in [25], however, their scheme is only first-order in time, and its computational cost is relatively expensive due to the nonlinear nature.

Therefore, in this paper, we aim to develop an efficient scheme for solving the full hydrodynamically coupled three components Cahn-Hilliard model. More precisely, we expect a linear scheme that can possess the unconditional energy stability and second-order accuracy. To this aim, except the numerical difficulties induced by those coupled and nonlinear terms in the bulk potentials, one needs to solve two more challenges including (i) the nonlinear coupling between the velocity and phase function through the convective and stress terms; and (ii) the coupling of the velocity and pressure through the incompressibility constraint. We combine the IEQ approach with the stabilization technique to discretize the nonlinear terms in the Cahn-Hilliard equations, the projection method for the Navier-Stokes equations to decouple the velocity and pressure, and a subtle implicit-explicit treatment to handle the stress and convective terms. Hence, at each time step, one only needs to solve a linear elliptic system for the phase-field variables and the velocity field, and a Poisson equation for the pressure. We give rigorous proofs of the well-posedness of the linear system together with the energy stability, and further demonstrate the stability and accuracy numerically in simulating some classical benchmark numerical examples in 2D and 3D.

The rest of the paper is organized as follows. In Section 2, we briefly describe the hydrodynamically coupled three components Cahn-Hilliard phase-field model and derive its associated PDE energy dissipation law. In Section 3, we present the numerical scheme and prove the well-posedness of the semi-discretized linear system and its discrete energy dissipation law rigorously. In section 4, we present various numerical examples to illustrate the accuracy and efficiency of the proposed schemes. Some concluding remarks are given in Section 5.

## 2. Model system

We now give a brief introduction to the Cahn-Hilliard phase-field model for the three components fluid flows system that was proposed in [4–6]. Suppose  $\Omega$  be a smooth, open bounded, connected domain in  $\mathbb{R}^d$ ,  $d = 2, 3$ . Let  $\phi_i$  ( $i = 1, 2, 3$ ) be the  $i$ -th phase-field variable which represents the volume fraction of the  $i$ -th component in the fluid mixture, i.e.,

$$\phi_i = \begin{cases} 1 & \text{inside the } i\text{-th component,} \\ 0 & \text{outside the } i\text{-th component.} \end{cases} \quad (2.1)$$

A smooth layer with the thickness  $\epsilon$  is used to connect the interface between 0 and 1. Assuming the mixture being perfect (no volume leaking), thus the three unknowns  $\phi_1, \phi_2, \phi_3$  are linked though the relationship as

$$\phi_1 + \phi_2 + \phi_3 = 1. \quad (2.2)$$

This is the link condition for the vector  $\mathbf{C} = (\phi_1, \phi_2, \phi_3)$ , where it belongs to the hyperplane of

$$\mathcal{S} = \{\mathbf{C} = (\phi_1, \phi_2, \phi_3) \in \mathbb{R}^3, \phi_1 + \phi_2 + \phi_3 = 1\}. \quad (2.3)$$

There exist several generalizations from the two-phasic model to the three-phasic model (cf. [4–6,19]). In this paper, we adopt below the approach in [4–6] and define the total free energy as

$$E(\phi_1, \phi_2, \phi_3) = \int_{\Omega} \left( \frac{3\epsilon}{8} L(\phi_1, \phi_2, \phi_3) + \frac{12}{\epsilon} F(\phi_1, \phi_2, \phi_3) \right) d\mathbf{x}, \quad (2.4)$$

where  $\epsilon$  is the order parameter to characterize the interfacial width,  $L(\phi_1, \phi_2, \phi_3)$  is the linear part, and  $F(\phi_1, \phi_2, \phi_3)$  is the nonlinear part.

The linear part is set as

$$L(\phi_1, \phi_2, \phi_3) = \Sigma_1 |\nabla \phi_1|^2 + \Sigma_2 |\nabla \phi_2|^2 + \Sigma_3 |\nabla \phi_3|^2, \quad (2.5)$$

where the coefficient  $\Sigma_i$  is called the “spreading” coefficient of the phase  $i$  at the interface between phases  $j$  and  $k$ . To be algebraically consistent with the two-phasic systems, the three surface tension parameters  $\sigma_{ij}$  ( $\sigma_{12}, \sigma_{13}, \sigma_{23}$ ) should verify the following conditions:

$$\Sigma_i = \sigma_{ij} + \sigma_{ik} - \sigma_{jk}, \quad i = 1, 2, 3. \tag{2.6}$$

Note  $\Sigma_i$  might not be always positive. If  $\Sigma_i > 0$ , the spreading is said to be “partial”, and if  $\Sigma_i < 0$ , it is called “total”.

The nonlinear potential  $F(\phi_1, \phi_2, \phi_3)$  given in [4–6] reads as:

$$F(\phi_1, \phi_2, \phi_3) = \sigma_{12}\phi_1^2\phi_2^2 + \sigma_{13}\phi_1^2\phi_3^2 + \sigma_{23}\phi_2^2\phi_3^2 + \phi_1\phi_2\phi_3(\Sigma_1\phi_1 + \Sigma_2\phi_2 + \Sigma_3\phi_3) + 3\Lambda\phi_1^2\phi_2^2\phi_3^2. \tag{2.7}$$

Since  $\phi_1, \phi_2, \phi_3$  satisfy the hyperplane link condition (2.2),  $F(\phi_1, \phi_2, \phi_3)$  can be rewritten as

$$F(\phi_1, \phi_2, \phi_3) = F_0(\phi_1, \phi_2, \phi_3) + P(\phi_1, \phi_2, \phi_3), \tag{2.8}$$

where

$$\begin{cases} F_0(\phi_1, \phi_2, \phi_3) = \frac{\Sigma_1}{2}\phi_1^2(1 - \phi_1)^2 + \frac{\Sigma_2}{2}\phi_2^2(1 - \phi_2)^2 + \frac{\Sigma_3}{2}\phi_3^2(1 - \phi_3)^2, \\ P(\phi_1, \phi_2, \phi_3) = 3\Lambda\phi_1^2\phi_2^2\phi_3^2, \end{cases}$$

and  $\Lambda$  is a non-negative constant.

The following lemmas hold (cf. [4]):

**Lemma 2.1.** For any  $\xi_1 + \xi_2 + \xi_3 = 0$ , there exists a constant  $\underline{\Sigma} > 0$  such that

$$\Sigma_1|\xi_1|^2 + \Sigma_2|\xi_2|^2 + \Sigma_3|\xi_3|^2 \geq \underline{\Sigma}(|\xi_1|^2 + |\xi_2|^2 + |\xi_3|^2), \tag{2.9}$$

if and only if the following condition holds:

$$\Sigma_1\Sigma_2 + \Sigma_1\Sigma_3 + \Sigma_2\Sigma_3 > 0, \quad \Sigma_i + \Sigma_j > 0, \quad \forall i \neq j. \tag{2.10}$$

**Lemma 2.2.** Let  $\sigma_{12}, \sigma_{13}$  and  $\sigma_{23}$  be three positive numbers and  $\Sigma_1, \Sigma_2$  and  $\Sigma_3$  defined by (2.6). (Note  $\Sigma_i$  might not be positive for some  $i$ .) For any  $\Lambda > 0$ , the bulk free energy  $F(\phi_1, \phi_2, \phi_3)$  defined in (2.8) is bounded from below if  $\phi_1, \phi_2, \phi_3$  is on the hyperplane  $S$  in 2D. Furthermore, the lower bound only depends on  $\Sigma_1, \Sigma_2, \Sigma_3$  and  $\Lambda$ .

**Remark 2.1.** From Lemma 2.1, when (2.10) holds, the summation of the gradient entropy term is bounded from below since  $\nabla(\phi_1 + \phi_2 + \phi_3) = 0$ , i.e.,

$$\sum_{i=1}^3 \Sigma_i \|\nabla\phi_i\|^2 \geq \underline{\Sigma} \sum_{i=1}^3 \|\nabla\phi_i\|^2 \geq 0. \tag{2.11}$$

**Remark 2.2.** The bulk part energy  $F(\phi_1, \phi_2, \phi_3)$  defined in (2.8) has to be bounded from below in order to form a meaningful physical system. For partial spreading case ( $\Sigma_i > 0, \forall i$ ), one can drop the six order polynomial term by assuming  $\Lambda = 0$  since  $F_0(\phi_1, \phi_2, \phi_3) \geq 0$  is naturally satisfied. For the total spreading case,  $\Lambda$  has to be non-zero. Moreover, to ensure the non-negativity for  $F$ ,  $\Lambda$  has to be large enough.

For 3D case, it is shown in [4] that the bulk energy  $F$  is bounded from below when  $P(\phi_1, \phi_2, \phi_3)$  takes the following form:

$$P(\phi_1, \phi_2, \phi_3) = 3\Lambda\phi_1^2\phi_2^2\phi_3^2(\phi_\alpha(\phi_1) + \phi_\alpha(\phi_2) + \phi_\alpha(\phi_3)) \tag{2.12}$$

where  $\phi_\alpha(x) = \frac{1}{(1+x^2)^\alpha}$  with  $0 < \alpha \leq \frac{8}{17}$ .

Since (2.8) is commonly used in literatures (cf. [4,6]), we adopt it as well for convenience. Nonetheless, it will be clear that the numerical schemes we develop in this paper can deal with either (2.8) or (2.12) without any essential difficulties.

When coupling with the hydrodynamics, the total free energy becomes

$$E_{tot}(\mathbf{u}, \phi_1, \phi_2, \phi_3) = \int_{\Omega} \left( \frac{1}{2}|\mathbf{u}|^2 + \frac{3\epsilon}{8}L(\phi_1, \phi_2, \phi_3) + \frac{12}{\epsilon}F(\phi_1, \phi_2, \phi_3) \right) d\mathbf{x}, \tag{2.13}$$

where  $\mathbf{u}$  is the fluid velocity.

Assuming that the fluid is incompressible and follows a generalized Fick's law that the mass flux be proportional to the gradient of the chemical potential, we can derive the following hydrodynamically coupled Cahn-Hilliard model:

$$\partial_t \phi_i + \nabla \cdot (\mathbf{u} \phi_i) = M \Delta \frac{\mu_i}{\Sigma_i}, \tag{2.14}$$

$$\mu_i = -\frac{3}{4} \epsilon \Sigma_i \Delta \phi_i + \frac{12}{\epsilon} (f_i + \beta_L), \quad i = 1, 2, 3, \tag{2.15}$$

$$\mathbf{u}_t + \mathbf{u} \cdot \nabla \mathbf{u} - \nu \Delta \mathbf{u} + \nabla p + \sum_{i=1}^3 \phi_i \nabla \mu_i = \mathbf{0}, \tag{2.16}$$

$$\nabla \cdot \mathbf{u} = 0, \tag{2.17}$$

where  $M$  is the mobility parameter,  $f_i = \partial_{\phi_i} F$ ,  $p$  is the pressure,  $\nu$  is the fluid viscosity,  $\beta_L$  is the Lagrange multiplier to ensure the hyperplane link condition (2.2) and it can be derived as

$$\beta_L = -\frac{1}{\Sigma_T} \left( \frac{f_1}{\Sigma_1} + \frac{f_2}{\Sigma_2} + \frac{f_3}{\Sigma_3} \right), \tag{2.18}$$

with

$$\frac{1}{\Sigma_T} = \frac{1}{\Sigma_1} + \frac{1}{\Sigma_2} + \frac{1}{\Sigma_3}. \tag{2.19}$$

The initial conditions read as

$$\mathbf{u}|_{(t=0)} = \mathbf{u}^0, \quad \phi_i|_{(t=0)} = \phi_i^0, \tag{2.20}$$

where the initial condition also satisfies  $\phi_1^0 + \phi_2^0 + \phi_3^0 = 1$ .

The convective term  $\nabla \cdot (\mathbf{u} \phi_i)$  in (2.14) takes the so-called *conservative* form as the two-phasic model, see [30,44]. The conservative formulation can ensure the volume conservation for each phase that can be easily derived if one takes the  $L^2$ -inner product with 1 for (2.14). By taking the summation for (2.14) for  $i = 1, 2, 3$  and using the hyperplane link condition (2.2), this term becomes  $\nabla \cdot \mathbf{u}$  which is zero for the continuous case. However, when developing numerical schemes, the velocity used to discretize the convective term may not follow the divergence-free condition leading to a consequence that the numerical solutions of  $\phi_i$  violate the hyperplane link condition (2.2).

To overcome this issue, we further rewrite the system (2.14)-(2.17) into the following equivalent form (cf. [25]).

$$\partial_t \phi_i + \nabla \cdot (\mathbf{u}(\phi_i - \bar{\phi}_i^0)) = M \Delta \frac{\mu_i}{\Sigma_i}, \tag{2.21}$$

$$\mu_i = -\frac{3}{4} \epsilon \Sigma_i \Delta \phi_i + \frac{12}{\epsilon} (f_i + \beta_L), \quad i = 1, 2, 3, \tag{2.22}$$

$$\mathbf{u}_t + \mathbf{u} \cdot \nabla \mathbf{u} - \nu \Delta \mathbf{u} + \nabla p + \sum_{i=1}^3 (\phi_i - \bar{\phi}_i^0) \nabla \mu_i = \mathbf{0}, \tag{2.23}$$

$$\nabla \cdot \mathbf{u} = 0, \tag{2.24}$$

where  $\bar{\phi}_i^0 = \frac{1}{|\Omega|} \int_{\Omega} \phi_i^0 d\mathbf{x}$ . Note  $\phi_1^0 + \phi_2^0 + \phi_3^0 = 1$ , then we derive

$$\bar{\phi}_1^0 + \bar{\phi}_2^0 + \bar{\phi}_3^0 = 1. \tag{2.25}$$

While the convective term in (2.21) and the stress term in (2.23) are slightly different with their original forms in (2.14) and (2.16), the new system (2.21)-(2.24) is actually equivalent to the original system (2.14)-(2.17). This is because the convective term in (2.21) can be written as

$$\nabla \cdot (\mathbf{u}(\phi_i - \bar{\phi}_i^0)) = \nabla \cdot (\mathbf{u} \phi_i) - \bar{\phi}_i^0 \nabla \cdot \mathbf{u} = \nabla \cdot (\mathbf{u} \phi_i) \tag{2.26}$$

from  $\nabla \cdot \mathbf{u} = 0$ , and the stress term in (2.23) is written as

$$\sum_{i=1}^3 (\phi_i - \bar{\phi}_i^0) \nabla \mu_i = \sum_{i=1}^3 \phi_i \nabla \mu_i - \nabla \cdot \left( \sum_{i=1}^3 \bar{\phi}_i^0 \mu_i \right) \tag{2.27}$$

where the latter gradient term can be absorbed into the pressure gradient directly.

**Remark 2.3.** There is some advantage by taking the formulation (2.21)-(2.24) that is, the summation of three convective terms  $\sum_{i=1}^3 \nabla \cdot (\mathbf{u}(\phi_i - \bar{\phi}_i^0))$  vanishes because  $\sum_{i=1}^3 (\phi_i - \bar{\phi}_i^0) = \sum_{i=1}^3 \phi_i - \sum_{i=1}^3 \bar{\phi}_i^0 = 1 - 1 = 0$  as long as the hyperplane link condition is always valid for  $\phi_i$  even though  $\nabla \cdot \mathbf{u} \neq 0$ . Namely, the new form of convective terms in (2.21) can help to ensure the hyperplane link condition  $\sum_{i=1}^3 \phi_i = 1$  even if the velocity field may not follow the divergence-free condition when developing algorithms.

**Remark 2.4.** The system (2.21)-(2.24) is equivalent to the following two phase-field variables system

$$\begin{cases} \partial_t \phi_i + \nabla \cdot (\mathbf{u}(\phi_i - \bar{\phi}_i^0)) = M \Delta \frac{\mu_i}{\Sigma_i}, \\ \mu_i = -\frac{3}{4} \epsilon \Sigma_i \Delta \phi_i + \frac{12}{\epsilon} (f_i + \beta_L), \quad i = 1, 2, \end{cases} \tag{2.28}$$

where  $\phi_3$  and  $\mu_3$  are given by the following explicit formula:

$$\phi_1 + \phi_2 + \phi_3 = 1, \tag{2.29}$$

$$\frac{\mu_1}{\Sigma_1} + \frac{\mu_2}{\Sigma_2} + \frac{\mu_3}{\Sigma_3} = 0. \tag{2.30}$$

Since the proof is quite similar to Theorem 3.1, we omit the details here.

We consider in this paper either of the two type boundary conditions below:

$$(i) \text{ all variables are periodic, or } (ii) \mathbf{u}|_{\partial\Omega} = \partial_{\mathbf{n}}\phi_i|_{\partial\Omega} = \partial_{\mathbf{n}}\mu_i|_{\partial\Omega}, \quad i = 1, 2, 3, \tag{2.31}$$

where  $\mathbf{n}$  is the unit outward normal on the boundary  $\partial\Omega$ .

The model equations (2.21)-(2.24) follow a dissipative energy law. By taking the  $L^2$  inner product of (2.14) with  $\mu_i$ , of (2.15) with  $-\partial_t \phi_i$ , of (2.16) with  $\mathbf{u}$ , and performing integration by parts, we can obtain

$$(\partial_t \phi_i, \mu_i) - (\mathbf{u}(\phi_i - \bar{\phi}_i^0), \nabla \mu_i) = -M \Sigma_i \left\| \frac{\nabla \mu_i}{\Sigma_i} \right\|^2, \tag{2.32}$$

$$-(\mu_i, \partial_t \phi_i) = -\frac{3}{4} \epsilon \Sigma_i d_t \|\nabla \phi_i\|^2 - \frac{12}{\epsilon} (f_i + \beta_L, \partial_t \phi_i), \tag{2.33}$$

$$\frac{1}{2} d_t \|\mathbf{u}\|^2 + \nu \|\nabla \mathbf{u}\|^2 - (p, \nabla \cdot \mathbf{u}) + \sum_{i=1}^3 ((\phi_i - \bar{\phi}_i^0) \nabla \mu_i, \mathbf{u}) = 0. \tag{2.34}$$

Then, by taking the summation of (2.32), (2.33), and (2.34) for  $i = 1, 2, 3$ , using (2.17) for the pressure term and using that  $(\beta_L, (\phi_1 + \phi_2 + \phi_3)_t) = (\beta_L, (1)_t) = 0$  due to Remark 2.4, we obtain the energy dissipative law as

$$\begin{aligned} & \frac{d}{dt} E_{tot}(\mathbf{u}, \phi_1, \phi_2, \phi_3) \\ &= -\nu \|\nabla \mathbf{u}\|^2 - M \left( \Sigma_1 \left\| \frac{\nabla \mu_1}{\Sigma_1} \right\|^2 + \Sigma_2 \left\| \frac{\nabla \mu_2}{\Sigma_2} \right\|^2 + \Sigma_3 \left\| \frac{\nabla \mu_3}{\Sigma_3} \right\|^2 \right) \\ &\leq -\nu \|\nabla \mathbf{u}\|^2 - M \underline{\Sigma} \left( \left\| \frac{\nabla \mu_1}{\Sigma_1} \right\|^2 + \left\| \frac{\nabla \mu_2}{\Sigma_2} \right\|^2 + \left\| \frac{\nabla \mu_3}{\Sigma_3} \right\|^2 \right), \end{aligned} \tag{2.35}$$

where the last inequality is derived by using the Lemma 2.1 since  $(\mu_1, \mu_2, \mu_3)$  satisfies the condition (2.30).

### 3. Numerical schemes

We now develop numerical schemes for solving the model (2.21)-(2.24) in this section. While we consider only time discretizations here, the results can carry over to any consistent finite-dimensional Galerkin approximations (finite elements or spectral) since the proof is based on variational formulations with all test functions in the same space as the trial function.

We aim to construct efficient schemes with some desired properties like linear, second-order accurate, and unconditionally energy stable. There are several numerical challenges needed to be overcome, including (i) how to decouple the computations of velocity and pressure; (ii) how to discretize the nonlinear term associated with the double-well potential  $F_0$ , the sixth-order polynomial potential as well as the Lagrange multiplier term especially; and (iii) how to develop proper discretizations for convective (in (2.14)) and stress terms (in (2.16)). Here we combine the newly developed IEQ approach with the stabilization technique to discretize the nonlinear terms as well as the projection method for the Navier-Stokes equations. For their coupled nonlinear terms, we discretize them by using the implicit-explicit combination. Remarkably,

the extra added linear stabilization term is particularly effective to improve the energy stability while keeping the required accuracy. The detailed procedure to develop the scheme is presented as follows.

We define an auxiliary function  $U(\mathbf{x}, t)$  as

$$U = \sqrt{F(\phi_1, \phi_2, \phi_3) + B}, \tag{3.1}$$

where  $B$  is any constant that ensures the radicand positive (in all numerical examples, we let  $B = 10$ ). Hence the total free energy (2.4) can be rewritten as

$$E_{tot}(\mathbf{u}, \phi_1, \phi_2, \phi_3, U) = \int_{\Omega} \left( \frac{1}{2} |\mathbf{u}|^2 + \frac{3}{8} L(\phi_1, \phi_2, \phi_3) + \frac{12}{\epsilon} U^2 \right) d\mathbf{x} - \frac{12}{\epsilon} B |\Omega|. \tag{3.2}$$

Then, we rewrite the system (2.21)-(2.24) to the following equivalent form with unknown variables  $(\mathbf{u}, p, \phi_i, \mu_i, U)$ :

$$\partial_t \phi_i + \nabla \cdot (\mathbf{u}(\phi_i - \bar{\phi}_i^0)) = M \Delta \frac{\mu_i}{\Sigma_i}, \tag{3.3}$$

$$\mu_i = -\frac{3}{4} \epsilon \Sigma_i \Delta \phi_i + \frac{12}{\epsilon} (H_i + \beta) U, \quad i = 1, 2, 3, \tag{3.4}$$

$$U_t = \frac{1}{2} \sum_{i=1}^3 H_i \partial_t \phi_i, \tag{3.5}$$

$$\mathbf{u}_t + \mathbf{u} \cdot \nabla \mathbf{u} - \nu \Delta \mathbf{u} + \nabla p + \sum_{i=1}^3 (\phi_i - \bar{\phi}_i^0) \nabla \mu_i = 0, \tag{3.6}$$

$$\nabla \cdot \mathbf{u} = 0, \tag{3.7}$$

where

$$\beta = -\frac{1}{\Sigma_T} \left( \frac{H_1}{\Sigma_1} + \frac{H_2}{\Sigma_2} + \frac{H_3}{\Sigma_3} \right), \tag{3.8}$$

$$H_i = \frac{f_i}{\sqrt{F(\phi_1, \phi_2, \phi_3) + B}}. \tag{3.9}$$

Note (3.8) can be also written as the following form,

$$\frac{H_1 + \beta}{\Sigma_1} + \frac{H_2 + \beta}{\Sigma_2} + \frac{H_3 + \beta}{\Sigma_3} = 0. \tag{3.10}$$

The transformed system (3.3)-(3.7) in terms with the variables  $(\phi_i, \mu_i, U, p)$  form a closed PDE system with the following initial conditions,

$$\begin{cases} \mathbf{u}|_{(t=0)} = \mathbf{u}^0, p|_{(t=0)} = p^0, \phi_i|_{(t=0)} = \phi_i^0, i = 1, 2, 3, \\ U|_{(t=0)} = U^0 = \sqrt{F(\phi_1^0, \phi_2^0, \phi_3^0) + B}. \end{cases} \tag{3.11}$$

Note the boundary conditions for  $U$  are not needed at all since the equation (3.5) is only an ODE with time. Thus the boundary conditions of the new system (3.3)-(3.7) are still (2.31).

Moreover, the equations (3.3)-(3.4) can be proved to be equivalent to the following system with two order parameters  $(\phi_1, \phi_2)$ :

$$\begin{cases} \partial_t \phi_i + \nabla \cdot (\mathbf{u}(\phi_i - \bar{\phi}_i^0)) = \frac{M}{\Sigma_i} \Delta \mu_i, \\ \mu_i = -\frac{3}{4} \epsilon \Sigma_i \Delta \phi_i + \frac{12}{\epsilon} (H_i + \beta) U, \quad i = 1, 2, \end{cases} \tag{3.12}$$

with

$$\phi_3 = 1 - \phi_1 - \phi_2, \quad \frac{\mu_3}{\Sigma_3} = -\left( \frac{\mu_1}{\Sigma_1} + \frac{\mu_2}{\Sigma_2} \right). \tag{3.13}$$

Since the corresponding proof is quite similar to Theorem 3.1, we omit the details here.

Let  $\delta t > 0$  denote the time step size and set  $t^n = n \delta t$  for  $0 \leq n \leq N$  with  $T = N \delta t$ . We also denote by  $(f(\mathbf{x}), g(\mathbf{x})) = \int_{\Omega} f(\mathbf{x})g(\mathbf{x})d\mathbf{x}$  the  $L^2$  inner product of any two functions  $f(\mathbf{x})$  and  $g(\mathbf{x})$ , and by  $\|f\| = \sqrt{(f, f)}$  the  $L^2$  norm of the function  $f(\mathbf{x})$ .

Using the second-order backward differentiation formula (BDF2), we now construct a time marching scheme to discretize the new system (3.3)-(3.7), that includes the following two steps:

*Step 1:* we compute  $\tilde{\mathbf{u}}^{n+1}, \phi_i^{n+1}, \mu_i^{n+1}, U^{n+1}$  by

$$\frac{3\tilde{\mathbf{u}}^{n+1} - 4\mathbf{u}^n + \mathbf{u}^{n-1}}{2\delta t} + \mathbf{B}(\mathbf{u}^*, \tilde{\mathbf{u}}^{n+1}) - \nu \Delta \tilde{\mathbf{u}}^{n+1} + \nabla p^n + \sum_{i=1}^3 (\phi_i^* - \bar{\phi}_i^0) \nabla \mu_i^{n+1} = 0, \quad (3.14)$$

$$\frac{3\phi_i^{n+1} - 4\phi_i^n + \phi_i^{n-1}}{2\delta t} + \nabla \cdot (\tilde{\mathbf{u}}^{n+1} (\phi_i^* - \bar{\phi}_i^0)) = M \Delta \frac{\mu_i^{n+1}}{\Sigma_i}, i = 1, 2, 3, \quad (3.15)$$

$$\mu_i^{n+1} = -\frac{3}{4} \epsilon \Sigma_i \Delta \phi_i^{n+1} + \frac{12}{\epsilon} (H_i^* + \beta^*) U^{n+1} + \frac{S}{\epsilon} \Sigma_i (\phi_i^{n+1} - \phi_i^*), \quad (3.16)$$

$$3U^{n+1} - 4U^n + U^{n-1} = \frac{1}{2} \sum_{i=1}^3 H_i^* (3\phi_i^{n+1} - 4\phi_i^n + \phi_i^{n-1}), \quad (3.17)$$

where

$$\begin{cases} \mathbf{B}(\mathbf{u}, \mathbf{v}) = (\mathbf{u} \cdot \nabla) \mathbf{v} + \frac{1}{2} (\nabla \cdot \mathbf{u}) \mathbf{v}, \\ \mathbf{u}^* = 2\mathbf{u}^n - \mathbf{u}^{n-1}, \phi_i^* = 2\phi_i^n - \phi_i^{n-1}, H_i^* = H(\phi_1^*, \phi_2^*, \phi_3^*), \\ \beta^* = -\frac{1}{\Sigma_T} \left( \frac{H_1^*}{\Sigma_1} + \frac{H_2^*}{\Sigma_2} + \frac{H_3^*}{\Sigma_3} \right), \end{cases} \quad (3.18)$$

$S$  is a positive stabilization parameter, and the boundary conditions are either periodic or

$$\tilde{\mathbf{u}}^{n+1}|_{\partial\Omega} = \partial_{\mathbf{n}} \phi_i^{n+1}|_{\partial\Omega} = \partial_{\mathbf{n}} \mu_i^{n+1}|_{\partial\Omega} = 0. \quad (3.19)$$

*Step 2:* we compute  $p^{n+1}, \mathbf{u}^{n+1}$  as follows,

$$\frac{3}{2\delta t} (\mathbf{u}^{n+1} - \tilde{\mathbf{u}}^{n+1}) + \nabla (p^{n+1} - p^n) = 0, \quad (3.20)$$

$$\nabla \cdot \mathbf{u}^{n+1} = 0, \quad (3.21)$$

where the boundary condition is either periodic or

$$\mathbf{u}^{n+1} \cdot \mathbf{n}|_{\partial\Omega} = 0. \quad (3.22)$$

**Remark 3.1.** We add an extra linear, second-order stabilization term associated with  $S$  in (3.12). This term introduces an error in the scale of  $S\delta t^2 \phi_{tt}(\cdot)$  which is comparable with the error introduced by the second-order extrapolation of the nonlinear term. In Section 4, we present enough numerical evidence to show that this stabilizer is critical to maintain the accuracy and improve the energy stability while using large time steps, see the accuracy/stability tests shown in Fig. 4.1 and 4.2. Similar treatment had been used to apply the IEQ/SAV method for various gradient flow models, see [7,8,31,45].

**Remark 3.2.**  $\mathbf{B}(\mathbf{u}, \mathbf{v})$  is the skew-symmetric form of the nonlinear advection term in the Navier–Stokes equation. Even though  $\nabla \cdot \mathbf{u} \neq 0$ , the identity  $(\mathbf{B}(\mathbf{u}, \mathbf{v}), \mathbf{v}) = 0$  still holds as long as the boundary condition  $\mathbf{u} \cdot \mathbf{n}|_{\partial\Omega} = 0$  is valid, which helps to preserve the discrete energy stability.

**Remark 3.3.** The computations of  $(\phi_i^{n+1}, \mu_i^{n+1}, \tilde{\mathbf{u}}^{n+1})$  and the pressure  $p^{n+1}$  are totally decoupled via a second-order pressure correction scheme [33] and a subtle implicit-explicit treatment for the stress and convective terms. It is quite an open problem on how to develop a second-order scheme that can decouple the computations of  $(\phi_i, \mu_i)$  from the velocity field  $\mathbf{u}$ . All decoupled type energy stable schemes were first-order accurate in time (cf. [21,25,29,30,32]).

**Remark 3.4.** The computations of the second-order scheme (3.14)-(3.22) need the values of  $\phi_i^1, U^1, p^1, u^1$ . In practice, we obtain these values by the following first-order scheme that reads as,

*Step 1:* we compute  $\tilde{\mathbf{u}}^1, \phi_i^1, \mu_i^1, U^1$  by

$$\frac{\tilde{\mathbf{u}}^1 - \mathbf{u}^0}{2\delta t} + \mathbf{B}(\mathbf{u}^0, \tilde{\mathbf{u}}^1) - \nu \Delta \tilde{\mathbf{u}}^1 + \nabla p^0 + \sum_{i=1}^3 (\phi_i^0 - \bar{\phi}_i^0) \nabla \mu_i^1 = 0, \quad (3.23)$$

$$\frac{\phi_i^1 - \phi_i^0}{\delta t} + \nabla \cdot (\tilde{\mathbf{u}}^1 (\phi_i^0 - \bar{\phi}_i^0)) = M \Delta \frac{\mu_i^1}{\Sigma_i}, i = 1, 2, 3, \quad (3.24)$$

$$\mu_i^1 = -\frac{3}{4}\epsilon \Sigma_i \Delta \phi_i^1 + \frac{12}{\epsilon} (H_i^0 + \beta^0) U^1 + \frac{S}{\epsilon} \Sigma_i (\phi_i^1 - \phi_i^0), \tag{3.25}$$

$$U^1 - U^0 = \frac{1}{2} \sum_{i=1}^3 H_i^0 (\phi_i^1 - \phi_i^0), \tag{3.26}$$

Step 2: we compute  $p^1, \mathbf{u}^1$  as follows,

$$\frac{1}{\delta t} (\mathbf{u}^1 - \tilde{\mathbf{u}}^1) + \nabla (p^1 - p^0) = 0, \tag{3.27}$$

$$\nabla \cdot \mathbf{u}^1 = 0. \tag{3.28}$$

The boundary condition for  $\tilde{\mathbf{u}}^1, \mathbf{u}^1, \phi_i^1, \mu_i^1$  follows the same boundary conditions as the scheme (3.14)-(3.22).

The following theorem ensures the numerical solutions  $(\phi_1^{n+1}, \phi_2^{n+1}, \phi_3^{n+1})$  always satisfies the hyperplane link condition  $\sum_{i=1}^3 \phi_i^{n+1} = 1$ , namely, no volume loss for the whole discrete scheme.

**Theorem 3.1.** *The system (3.15)-(3.16) is equivalent to the following scheme with two order parameters,*

$$\frac{3\phi_i^{n+1} - 4\phi_i^n + \phi_i^{n-1}}{2\delta t} + \nabla \cdot (\tilde{\mathbf{u}}^{n+1} (\phi_i^* - \bar{\phi}_i^0)) = M \Delta \frac{\mu_i^{n+1}}{\Sigma_i}, \tag{3.29}$$

$$\mu_i^{n+1} = -\frac{3}{4}\epsilon \Sigma_i \Delta \phi_i^{n+1} + \frac{12}{\epsilon} (H_i^* + \beta^*) U^{n+1} + \frac{S}{\epsilon} \Sigma_i (\phi_i^{n+1} - \phi_i^*), i = 1, 2, \tag{3.30}$$

with

$$\phi_3^{n+1} = 1 - \phi_1^{n+1} - \phi_2^{n+1}, \tag{3.31}$$

$$\frac{\mu_3^{n+1}}{\Sigma_3} = -\left(\frac{\mu_1^{n+1}}{\Sigma_1} + \frac{\mu_2^{n+1}}{\Sigma_2}\right). \tag{3.32}$$

**Proof.** First, we derive (3.15)-(3.16) by assuming that (3.29)-(3.32) are satisfied. Taking the summation of (3.29) for  $i = 1, 2$ , applying (3.31) at  $t = t^{n+1}, t^n, t^{n-1}$ , and using (3.32) and  $\sum_{i=1}^3 \bar{\phi}_i^0 = 1$ , we obtain

$$\frac{3\phi_3^{n+1} - 4\phi_3^n + \phi_3^{n-1}}{2\delta t} + \nabla \cdot (\tilde{\mathbf{u}}^{n+1} (\phi_3^* - \bar{\phi}_3^0)) = M \Delta \frac{\mu_3^{n+1}}{\Sigma_3}. \tag{3.33}$$

Furthermore, from (3.32), we derive

$$\begin{aligned} \mu_3^{n+1} &= -\Sigma_3 \left( \frac{\mu_1^{n+1}}{\Sigma_1} + \frac{\mu_2^{n+1}}{\Sigma_2} \right) \\ &= -\Sigma_3 \left( -\frac{3}{4}\epsilon \Delta \phi_1^{n+1} - \frac{3}{4}\epsilon \Delta \phi_2^{n+1} + \frac{12}{\epsilon} \left( \frac{H_1^* + \beta^*}{\Sigma_1} + \frac{H_2^* + \beta^*}{\Sigma_2} \right) U^{n+1} \right. \\ &\quad \left. + \frac{S}{\epsilon} (\phi_1^{n+1} + \phi_2^{n+1} - \phi_1^* + \phi_2^*) \right) \\ &= -\frac{3}{4}\epsilon \Sigma_3 \Delta \phi_3^{n+1} + \frac{12}{\epsilon} (H_3^* + \beta^*) U^{n+1} + \frac{S}{\epsilon} \Sigma_3 (\phi_3^{n+1} - \phi_3^*), \end{aligned}$$

where we use (3.31) and the definition of  $\beta^*$  in (3.18).

Second, we then assume that the equations (3.15)-(3.16) are satisfied and derive (3.29)-(3.32). We use the math induction and assume (3.31) are valid for  $t = t^n$  and  $t = t^{n-1}$  (the validity of (3.31) at  $t = t^1$  is shown in Remark 3.5). For any  $m$ , we define

$$C^m = \phi_1^m + \phi_2^m + \phi_3^m, \Theta^m = \frac{\mu_1^m}{\Sigma_1} + \frac{\mu_2^m}{\Sigma_2} + \frac{\mu_3^m}{\Sigma_3}. \tag{3.34}$$

By taking the summation of (3.15) for  $i = 1, 2, 3$ , we derive

$$\frac{3}{2\delta t} (C^{n+1} - 1) = M \Delta \Theta^{n+1}, \tag{3.35}$$

where the convective terms satisfy

$$\nabla \cdot (\tilde{\mathbf{u}}^{n+1} \sum_{i=1}^3 (\phi_i^* - \bar{\phi}_i^0)) = 0 \tag{3.36}$$

since  $\sum_{i=1}^3 \bar{\phi}_i^0 = 1$  and  $\sum_{i=1}^3 \phi_i^* = 1$  by the induction.

By taking the summation of (3.16) for  $i = 1, 2, 3$ , we derive

$$\Theta^{n+1} = -\frac{3}{4}\epsilon \Delta C^{n+1} + \frac{S}{\epsilon}(C^{n+1} - 1). \tag{3.37}$$

By taking the  $L^2$  inner product of (3.35) with  $-\frac{2\delta t}{3}\Theta^{n+1}$ , of (3.37) with  $C^{n+1} - 1$ , and taking the summation of the two obtained equalities, we derive

$$\frac{3}{4}\epsilon \|\nabla C^{n+1}\|^2 + \frac{S}{\epsilon} \|C^{n+1} - 1\|^2 + \frac{2\delta t}{3} M \|\nabla \Theta^{n+1}\|^2 = 0. \tag{3.38}$$

Since the left hand side of (3.38) is a sum of non-negative terms, thus  $\nabla C^{n+1} = 0$  and  $\nabla \Theta^{n+1} = 0$  that implies the functions  $C^{n+1}$  and  $\Theta^{n+1}$  are both constants. Then (3.35) leads to  $C^{n+1} = 1$  that means the (3.31) is valid. We also derive  $\Theta^{n+1} = 0$  from (3.37) that implies (3.32) is valid.  $\square$

**Remark 3.5.** The derivation of Theorem 3.1 in the second step lies on the math induction where we assume (3.31) is valid for step  $n$  and  $n - 1$ . Since (3.31) is valid for  $t = t^0$  automatically, we only need to show that it is also valid for  $t = t^1$ . That can be easily derived by performing the similar procedure as Theorem 3.1 for the scheme (3.24)-(3.25). The corresponding proof is quite similar to Theorem 3.1 thus we leave the details to the interested readers.

In practice, the new variable  $U^{n+1}$  is not needed to be solved explicitly. We can first rewrite (3.17) as

$$U^{n+1} = \frac{1}{2} \sum_{i=1}^3 H_i^* \phi_i^{n+1} + g^n, \tag{3.39}$$

where

$$g^n = \frac{4U^n - U^{n-1}}{3} - \frac{1}{2} \sum_{i=1}^3 H_i^* \frac{4\phi_i^n - \phi_i^{n-1}}{3}. \tag{3.40}$$

Thus the system (3.14)-(3.17) can be rewritten as

$$\tilde{\mathbf{u}}^{n+1} + \frac{2\delta t}{3} \mathbf{B}(\mathbf{u}^*, \tilde{\mathbf{u}}^{n+1}) - \frac{2\delta t}{3} \nu \Delta \tilde{\mathbf{u}}^{n+1} + \frac{2\delta t}{3} \sum_{i=1}^3 (\phi_i^* - \bar{\phi}_i^0) \nabla \mu_i^{n+1} = \mathbf{g}_1, \tag{3.41}$$

$$\phi_i^{n+1} + \frac{2\delta t}{3} \nabla \cdot (\tilde{\mathbf{u}}^{n+1} (\phi_i^* - \bar{\phi}_i^0)) - \frac{2\delta t}{3} M \Delta \frac{\mu_i^{n+1}}{\Sigma_i} = g_2^i, \tag{3.42}$$

$$-\mu_i^{n+1} - \frac{3}{4}\epsilon \Sigma_i \Delta \phi_i^{n+1} + \frac{6}{\epsilon} (H_i^* + \beta) \sum_{i=1}^3 H_i^* \phi_i^{n+1} + \frac{S}{\epsilon} \Sigma_i \phi_i^{n+1} = g_3^i, \tag{3.43}$$

where  $\mathbf{g}_1, g_2^i, g_3^i$  include all explicit terms in each corresponding equation. Note the new auxiliary variable  $U^{n+1}$  disappears in the above scheme, hence we solve the system (3.41)-(3.43) first and update  $U^{n+1}$  by (3.39).

We develop the associated weak form of the system (3.41)-(3.43) and show its well-posedness. For simplicity, the periodic boundary conditions are only considered in this paper. For the physical boundary conditions, the proof can be derived similarly without essential difficulties. We define three Sobolev spaces as follows,

$$H_{per}^k(\Omega) = \{\phi \in H^k(\Omega) : \phi \text{ is periodic}\},$$

$$\bar{H}^k(\Omega) = \{\phi \in H_{per}^k(\Omega) : \int_{\Omega} \phi d\mathbf{x} = 0\},$$

$$H_{\mathbf{u}}^k(\Omega) = \{\mathbf{u} \in [H_{per}^k(\Omega)]^d\}.$$

By integrating (3.42), we obtain

$$\int_{\Omega} \phi_i^{n+1} d\mathbf{x} = \int_{\Omega} \phi_i^n d\mathbf{x} = \dots = \int_{\Omega} \phi_i^0 d\mathbf{x}, \tag{3.44}$$

for  $i = 1, 2, 3$ . We let

$$\mathbf{u} = \bar{\mathbf{u}}^{n+1}, \phi_i = \phi_i^{n+1} - \frac{1}{|\Omega|} \int_{\Omega} \phi_i^0 d\mathbf{x}, \mu_i = \mu_i^{n+1} - \frac{1}{|\Omega|} \int_{\Omega} \mu_i^{n+1} d\mathbf{x}. \tag{3.45}$$

Hence we derive  $\phi_1 + \phi_2 + \phi_3 = 0$  from Theorem 3.1. The weak form of (3.41)-(3.43) can be formulated as follows.

Find  $\phi_i \in \bar{H}^1(\Omega)$ ,  $\mu_i \in \bar{H}^1(\Omega)$ ,  $\mathbf{u} \in H_{\mathbf{u}}^1(\Omega)$  via

$$(\mathbf{u}, \mathbf{v}) + \frac{2\delta t}{3} (\mathbf{B}(\mathbf{u}^*, \mathbf{u}), \mathbf{v}) + \frac{2\delta t}{3} \nu (\nabla \mathbf{u}, \nabla \mathbf{v}) + \frac{2\delta t}{3} \left( \sum_{i=1}^3 (\phi_i^* - \bar{\phi}_i^0) \nabla \mu_i, \mathbf{v} \right) = (\tilde{\mathbf{g}}_1, \mathbf{v}), \tag{3.46}$$

$$(\phi_i, w_i) - \frac{2\delta t}{3} (\mathbf{u}(\phi_i^* - \bar{\phi}_i^0), \nabla w_i) + \frac{2\delta t}{3} \frac{M}{\Sigma_i} (\nabla \mu_i, \nabla w_i) = (\tilde{g}_2^i, w_i), \tag{3.47}$$

$$-(\mu_i, \psi_i) + \frac{3}{4} \epsilon \Sigma_i (\nabla \phi_i, \nabla \psi_i) + \frac{6}{\epsilon} (H_i^* + \beta^*) \left( \sum_{i=1}^3 H_i^* \phi_i, \psi_i \right) + \frac{S}{\epsilon} \Sigma_i (\phi_i, \psi_i) = (\tilde{g}_3^i, \psi_i), \tag{3.48}$$

for any  $\psi_i \in \bar{H}^1(\Omega)$ ,  $w_i \in \bar{H}^1(\Omega)$ ,  $\mathbf{v} \in H_{\mathbf{u}}^1(\Omega)$ , where  $\tilde{\mathbf{g}}_1, \tilde{g}_2^i, \tilde{g}_3^i$  include corresponding explicit terms in each equation.

We denote the above linear system (3.46)-(3.48) as

$$(\mathbb{L}(\mathbf{X}), \mathbf{Y}) = (\mathbb{B}, \mathbf{Y}), \tag{3.49}$$

where  $\mathbf{X} = (\mathbf{u}, \mu_i, \phi_i)^T$ ,  $\mathbf{Y} = (\mathbf{v}, w_i, \psi_i)^T$ ,  $\mathbf{X}, \mathbf{Y} \in (H_{\mathbf{u}}^1, \bar{H}^1, \bar{H}^1)(\Omega)$ , and  $\mathbb{B} = (\tilde{\mathbf{g}}_1, g_2^i, g_3^i)^T$ .

Next, assuming that  $\psi^n$  and  $\psi^{n-1}$  for any variable  $\psi$  are known, we show the well-posedness of the linear system (3.49).

**Theorem 3.2.** *There exists a unique solution  $(\mathbf{u}, \mu_i, \phi_i) \in (H_{\mathbf{u}}^1, \bar{H}^1, \bar{H}^1)(\Omega)$  for the linear system (3.49).*

**Proof.** (i). By setting  $\mathbf{X} = (\mathbf{u}, \mu_i, \phi_i)^T$  and  $\mathbf{Y} = (\mathbf{v}, w_i, \psi_i)^T$  where  $\mathbf{X}, \mathbf{Y} \in (H_{\mathbf{u}}^1, \bar{H}^1, \bar{H}^1)(\Omega)$ , we obtain

$$(\mathbb{L}(\mathbf{X}), \mathbf{Y}) \leq C_1 \left( \|\mathbf{u}\|_{H^1} + \sum_{i=1}^3 \|\mu_i\|_{H^1} + \sum_{i=1}^3 \|\phi_i\|_{H^1} \right) \left( \|\mathbf{v}\|_{H^1} + \sum_{i=1}^3 \|w_i\|_{H^1} + \sum_{i=1}^3 \|\psi_i\|_{H^1} \right),$$

where  $C_1$  is some constant that may depend on  $\delta t, M, \Sigma_i, S, \epsilon, \|\nabla \mathbf{u}^*\|_{L^\infty}, \|\mathbf{u}^*\|_{L^\infty}, \|\phi_i^*\|_{L^\infty}, \|\phi_i^0\|_{L^\infty}, \|\beta^*\|_{L^\infty}$ , and  $\|H^*\|_{L^\infty}$ . This tells us that  $\mathbb{L}$  is bounded.

(ii). It is easy to find that

$$\begin{aligned} (\mathbb{L}(\mathbf{X}), \mathbf{X}) &= \|\mathbf{u}\|^2 + \frac{2\delta t}{3} \nu \|\nabla \mathbf{u}\|^2 \\ &\quad + \sum_{i=1}^3 \left( \frac{2\delta t}{3} M \Sigma_i \left\| \frac{\nabla \mu_i}{\Sigma_i} \right\|^2 + \frac{3}{4} \epsilon \Sigma_i \|\nabla \phi_i\|^2 + \frac{S}{\epsilon} \Sigma_i \|\phi_i\|^2 \right) + \frac{6}{\epsilon} \|H_1^* \phi_1 + H_2^* \phi_2 + H_3^* \phi_3\|^2 \\ &\geq \|\mathbf{u}\|^2 + \frac{2\delta t}{3} \nu \|\nabla \mathbf{u}\|^2 \\ &\quad + \sum_{i=1}^3 \left( \frac{2\delta t}{3} M \underline{\Sigma} \left\| \frac{\nabla \mu_i}{\Sigma_i} \right\|^2 + \frac{3}{4} \epsilon \underline{\Sigma} \|\nabla \phi_i\|^2 + \frac{S}{\epsilon} \underline{\Sigma} \|\phi_i\|^2 \right) + \frac{6}{\epsilon} \|H_1^* \phi_1 + H_2^* \phi_2 + H_3^* \phi_3\|^2 \\ &\geq C_2 \left( \|\mathbf{u}\|_{H^1}^2 + \sum_{i=1}^3 (\|\phi_i\|_{H^1}^2 + \|\mu_i\|_{H^1}^2) \right), \end{aligned}$$

where we use Lemma 2.1 since  $\sum_{i=1}^3 \frac{\nabla \mu_i}{\Sigma_i} = 0$  and  $\sum_{i=1}^3 \phi_i = 0$ . The constant  $C_2$  depends on  $\delta t, M, \underline{\Sigma}, \nu, S, \epsilon$ . This tells us that  $\mathbb{L}$  is coercive.

Therefore, we conclude that the linear system (3.49) admits a unique solution  $\mathbf{X} = (\mathbf{u}, \mu_i, \phi_i)^T \in (H_{\mathbf{u}}^1, \bar{H}^1, \bar{H}^1)(\Omega)$  by using the Lax-Milgram theorem.  $\square$

The unconditional energy stability of the scheme (3.14)-(3.22) is shown as follows.

**Theorem 3.3.** *The time-discrete scheme (3.14)-(3.22) satisfies the discrete energy dissipation law as follows*

$$\frac{1}{\delta t} (E^{n+1} - E^n) \leq -\nu \|\nabla \bar{\mathbf{u}}^{n+1}\|^2 - M \underline{\Sigma} \sum_{i=1}^3 \left\| \frac{\nabla \mu_i^{n+1}}{\Sigma_i} \right\|^2 \leq 0, \tag{3.50}$$

where

$$\begin{aligned}
 E^{n+1} = & \frac{1}{2} \left( \frac{1}{2} \|\mathbf{u}^{n+1}\|^2 + \frac{1}{2} \|2\mathbf{u}^{n+1} - \mathbf{u}^n\|^2 \right) + \frac{\delta t^2}{3} \|\nabla p^{n+1}\|^2 \\
 & + \frac{3\epsilon}{8} \sum_{i=1}^3 \left( \Sigma_i \left( \frac{1}{2} \|\nabla \phi_i^{n+1}\|^2 + \frac{1}{2} \|2\nabla \phi_i^{n+1} - \nabla \phi_i^n\|^2 \right) \right) \\
 & + \frac{12}{\epsilon} \left( \frac{1}{2} \|U^{n+1}\|^2 + \frac{1}{2} \|2U^{n+1} - U^n\|^2 \right) + \frac{S}{2\epsilon} \sum_{i=1}^3 (\Sigma_i \|\phi_i^{n+1} - \phi_i^n\|^2) \geq 0.
 \end{aligned} \tag{3.51}$$

**Proof.** By taking the inner product of (3.14) with  $2\delta t \tilde{\mathbf{u}}^{n+1}$  in the  $L^2$  space, we obtain

$$\begin{aligned}
 (3\tilde{\mathbf{u}}^{n+1} - 4\mathbf{u}^n + \mathbf{u}^{n-1}, \tilde{\mathbf{u}}^{n+1}) + 2\nu\delta t \|\nabla \tilde{\mathbf{u}}^{n+1}\|^2 + 2\delta t (\nabla p^n, \tilde{\mathbf{u}}^{n+1}) \\
 + 2\delta t \sum_{i=1}^3 \left( (\phi_i^* - \bar{\phi}_i^0) \nabla \mu_i^{n+1}, \tilde{\mathbf{u}}^{n+1} \right) = 0.
 \end{aligned} \tag{3.52}$$

From (3.20), for any variable  $\mathbf{v}$  with  $\nabla \cdot \mathbf{v} = 0$ , we have

$$(\mathbf{u}^{n+1}, \mathbf{v}) = (\tilde{\mathbf{u}}^{n+1}, \mathbf{v}). \tag{3.53}$$

We derive following equality

$$\begin{aligned}
 (3\tilde{\mathbf{u}}^{n+1} - 4\mathbf{u}^n + \mathbf{u}^{n-1}, \tilde{\mathbf{u}}^{n+1}) \\
 = (3\tilde{\mathbf{u}}^{n+1} - 4\mathbf{u}^n + \mathbf{u}^{n-1}, \mathbf{u}^{n+1}) + (3\tilde{\mathbf{u}}^{n+1} - 4\mathbf{u}^n + \mathbf{u}^{n-1}, \tilde{\mathbf{u}}^{n+1} - \mathbf{u}^{n+1}) \\
 = (3\mathbf{u}^{n+1} - 4\mathbf{u}^n + \mathbf{u}^{n-1}, \mathbf{u}^{n+1}) + (3\tilde{\mathbf{u}}^{n+1}, \tilde{\mathbf{u}}^{n+1} - \mathbf{u}^{n+1}) \\
 = (3\mathbf{u}^{n+1} - 4\mathbf{u}^n + \mathbf{u}^{n-1}, \mathbf{u}^{n+1}) + 3(\tilde{\mathbf{u}}^{n+1} - \mathbf{u}^{n+1}, \tilde{\mathbf{u}}^{n+1} + \mathbf{u}^{n+1}) \\
 = \frac{1}{2} \left( \|\mathbf{u}^{n+1}\|^2 - \|\mathbf{u}^n\|^2 + \|2\mathbf{u}^{n+1} - \mathbf{u}^n\|^2 - \|2\mathbf{u}^n - \mathbf{u}^{n-1}\|^2 \right. \\
 \left. + \|\mathbf{u}^{n+1} - 2\mathbf{u}^n + \mathbf{u}^{n-1}\|^2 \right) + 3(\|\tilde{\mathbf{u}}^{n+1}\|^2 - \|\mathbf{u}^{n+1}\|^2),
 \end{aligned} \tag{3.54}$$

where we use the following identity

$$2(3a - 4b + c, a) = a^2 - b^2 + (2a - b)^2 - (2b - c)^2 + (a - 2b + c)^2. \tag{3.55}$$

We reformulate the projection step (3.20) as

$$\frac{3}{2\delta t} \mathbf{u}^{n+1} + \nabla p^{n+1} = \frac{3}{2\delta t} \tilde{\mathbf{u}}^{n+1} + \nabla p^n. \tag{3.56}$$

By taking the square of both sides of the above equation, we get

$$\frac{9}{4\delta t^2} \|\mathbf{u}^{n+1}\|^2 + \|\nabla p^{n+1}\|^2 = \frac{9}{4\delta t^2} \|\tilde{\mathbf{u}}^{n+1}\|^2 + \|\nabla p^n\|^2 + \frac{3}{\delta t} (\tilde{\mathbf{u}}^{n+1}, \nabla p^n). \tag{3.57}$$

Hence, by multiplying  $2\delta t^2/3$  of the above equation, we derive

$$\frac{3}{2} (\|\mathbf{u}^{n+1}\|^2 - \|\tilde{\mathbf{u}}^{n+1}\|^2) + \frac{2\delta t^2}{3} (\|\nabla p^{n+1}\|^2 - \|\nabla p^n\|^2) = 2\delta t (\tilde{\mathbf{u}}^{n+1}, \nabla p^n). \tag{3.58}$$

By taking the inner product of (3.20) with  $2\delta t \mathbf{u}^{n+1}$  in the  $L^2$  space, we have

$$\frac{3}{2} (\|\mathbf{u}^{n+1}\|^2 - \|\tilde{\mathbf{u}}^{n+1}\|^2 + \|\mathbf{u}^{n+1} - \tilde{\mathbf{u}}^{n+1}\|^2) = 0. \tag{3.59}$$

We combine (3.52), (3.54), (3.58), and (3.59) to obtain

$$\begin{aligned}
 \frac{1}{2} (\|\mathbf{u}^{n+1}\|^2 - \|\mathbf{u}^n\|^2 + \|2\mathbf{u}^{n+1} - \mathbf{u}^n\|^2 - \|2\mathbf{u}^n - \mathbf{u}^{n-1}\|^2 + \|\mathbf{u}^{n+1} - 2\mathbf{u}^n + \mathbf{u}^{n-1}\|^2) \\
 + \frac{3}{2} \|\mathbf{u}^{n+1} - \tilde{\mathbf{u}}^{n+1}\|^2 + \frac{2\delta t^2}{3} (\|\nabla p^{n+1}\|^2 - \|\nabla p^n\|^2) + 2\nu\delta t \|\nabla \tilde{\mathbf{u}}^{n+1}\|^2 \\
 + 2\delta t \sum_{i=1}^3 \left( (\phi_i^* - \bar{\phi}_i^0) \nabla \mu_i^{n+1}, \tilde{\mathbf{u}}^{n+1} \right) = 0.
 \end{aligned} \tag{3.60}$$

Computing the inner product of (3.15) with  $2\delta t\mu_i^{n+1}$  in the  $L^2$  space, we have

$$(3\phi_i^{n+1} - 4\phi_i^n + \phi_i^{n-1}, \mu_i^{n+1}) - 2\delta t(\tilde{\mathbf{u}}^{n+1}(\phi_i^* - \bar{\phi}_i^0), \nabla\mu_i^{n+1}) + 2\delta tM\Sigma_i \left\| \frac{\nabla\mu_i^{n+1}}{\Sigma_i} \right\|^2 = 0. \tag{3.61}$$

Computing the  $L^2$  inner product of (3.16) with  $-(3\phi^{n+1} - 4\phi^n + \phi^{n-1})$ , we find

$$\begin{aligned} & -(\mu_i^{n+1}, 3\phi_i^{n+1} - 4\phi_i^n + \phi_i^{n-1}) \\ &= -\frac{3}{4}\epsilon\Sigma_i(\nabla\phi_i^{n+1}, \nabla(3\phi_i^{n+1} - 4\phi_i^n + \phi_i^{n-1})) \\ & \quad - \frac{12}{\epsilon}((H_i^* + \beta^*)U^{n+1}, 3\phi_i^{n+1} - 4\phi_i^n + \phi_i^{n-1}) \\ & \quad - \frac{S}{\epsilon}(\Sigma_i(\phi_i^{n+1} - \phi_i^*), 3\phi_i^{n+1} - 4\phi_i^n + \phi_i^{n-1}). \end{aligned} \tag{3.62}$$

We compute the inner product of (3.17) with  $\frac{24}{\epsilon}U^{n+1}$  in the  $L^2$  space and use (3.55) to obtain

$$\begin{aligned} & \frac{12}{\epsilon}(\|U^{n+1}\|^2 - \|U^n\|^2 + \|2U^{n+1} - U^n\|^2 - \|2U^n - U^{n-1}\|^2 \\ & \quad + \|U^{n+1} - 2U^n + U^{n-1}\|^2) = \frac{12}{\epsilon} \sum_{i=1}^3 (H_i^*(3\phi_i^{n+1} - 4\phi_i^n + \phi_i^{n-1}), U^{n+1}). \end{aligned} \tag{3.63}$$

Hence, by combining (3.60)-(3.63) and taking the summation for  $i = 1, 2, 3$ , we arrive at

$$\begin{aligned} & \frac{1}{2}(\|\mathbf{u}^{n+1}\|^2 - \|\mathbf{u}^n\|^2 + \|2\mathbf{u}^{n+1} - \mathbf{u}^n\|^2 - \|2\mathbf{u}^n - \mathbf{u}^{n-1}\|^2) + \frac{2\delta t^2}{3}(\|\nabla p^{n+1}\|^2 - \|\nabla p^n\|^2) \\ & \quad + \frac{3\epsilon}{8} \sum_{i=1}^3 (\Sigma_i(\|\nabla\phi_i^{n+1}\|^2 - \|\nabla\phi_i^n\|^2 + \|\nabla(2\phi_i^{n+1} - \phi_i^n)\|^2 - \|\nabla(2\phi_i^n - \phi_i^{n-1})\|^2)) \\ & \quad + \frac{12}{\epsilon}(\|U^{n+1}\|^2 - \|U^n\|^2 + \|2U^{n+1} - U^n\|^2 - \|2U^n - U^{n-1}\|^2) \\ & \quad + \frac{S}{\epsilon} \sum_{i=1}^3 (\Sigma_i(\|\phi_i^{n+1} - \phi_i^n\|^2 - \|\phi_i^n - \phi_i^{n-1}\|^2)) \\ & \quad + \left\{ \frac{1}{2}\|\mathbf{u}^{n+1} - 2\mathbf{u}^n + \mathbf{u}^{n-1}\|^2 + \frac{3}{2}\|\mathbf{u}^{n+1} - \tilde{\mathbf{u}}^{n+1}\|^2 \right. \\ & \quad \left. + \frac{3\epsilon}{8} \sum_{i=1}^3 \Sigma_i\|\nabla(\phi_i^{n+1} - 2\phi_i^n + \phi_i^{n-1})\|^2 + \frac{12}{\epsilon}\|U^{n+1} - 2U^n + U^{n-1}\|^2 \right. \\ & \quad \left. + \frac{2S}{\epsilon} \sum_{i=1}^3 \Sigma_i\|\phi_i^{n+1} - 2\phi_i^n + \phi_i^{n-1}\|^2 \right\} \\ &= -2\delta t\nu\|\nabla\tilde{\mathbf{u}}^{n+1}\|^2 - 2\delta tM \sum_{i=1}^3 \Sigma_i \left\| \frac{\nabla\mu_i^{n+1}}{\Sigma_i} \right\|^2 \\ &\leq -2\delta t\nu\|\nabla\tilde{\mathbf{u}}^{n+1}\|^2 - 2\delta tM\underline{\Sigma} \sum_{i=1}^3 \left\| \frac{\nabla\mu_i^{n+1}}{\Sigma_i} \right\|^2 \leq 0, \end{aligned} \tag{3.64}$$

where we use the following two identities

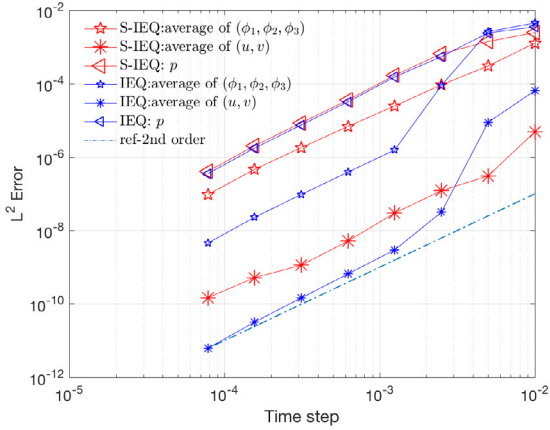
$$(3a - 4b + c)(a - 2b + c) = (a - b)^2 - (b - c)^2 + 2(a - 2b + c)^2, \tag{3.65}$$

and

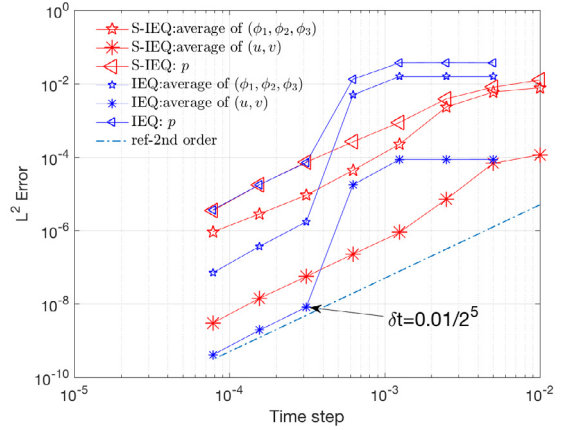
$$\sum_{i=1}^3 (\beta^*U^{n+1}, 3\phi_i^{n+1} - 4\phi_i^n + \phi_i^{n-1}) = (\beta^*U^{n+1}, \sum_{i=1}^3 (3\phi_i^{n+1} - 4\phi_i^n + \phi_i^{n-1})) = 0 \tag{3.66}$$

which is due to (3.31).

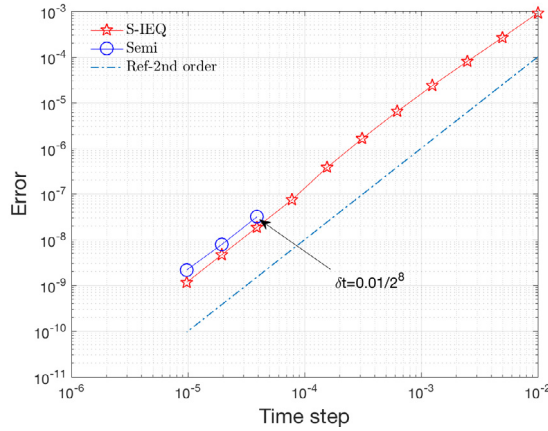
Finally, we obtain  $E^{n+1} \geq 0$  by using Lemma 2.1 and (3.31). Likewise, we obtain (3.50) after dropping the terms in  $\{ \}$  of (3.64) since they are positive, i.e.,



(a)  $(\sigma_{12}, \sigma_{13}, \sigma_{23}) = 0.02(1, 1, 1)$ .



(b)  $(\sigma_{12}, \sigma_{13}, \sigma_{23}) = 0.02(1, 1, 3)$ .



(c)  $(\sigma_{12}, \sigma_{13}, \sigma_{23}) = 0.02(1, 0.6, 0.6)$ .

**Fig. 4.1.** The average of the  $L^2$  numerical errors for the three phase-field variables  $(\phi_1, \phi_2, \phi_3)$ , the average of the two velocity components  $(u, v)$ , the pressure  $p$ , that are computed using the schemes S-IEQ (shown in (a)) and IEQ (shown in (b)) with various temporal resolutions. (c) The average of the  $L^2$  numerical errors for the three phase-field variables  $(\phi_1, \phi_2, \phi_3)$  computed by S-IEQ and the scheme Semi. Three sets of surface tension parameters are used respectively where (a)  $(\sigma_{12}, \sigma_{13}, \sigma_{23}) = 0.02(1, 1, 1)$ , (b)  $0.02(1, 1, 3)$ , and (c)  $0.02(1, 0.6, 0.6)$ .

$$\begin{aligned} \sum_{i=1}^3 \Sigma_i \|\nabla(\phi_i^{n+1} - 2\phi_i^n + \phi_i^{n-1})\|^2 &\geq \underline{\Sigma} \sum_{i=1}^3 \|\nabla(\phi_i^{n+1} - 2\phi_i^n + \phi_i^{n-1})\|^2 \geq 0, \\ \sum_{i=1}^3 \Sigma_i \|\phi_i^{n+1} - 2\phi_i^n + \phi_i^{n-1}\|^2 &\geq \underline{\Sigma} \sum_{i=1}^3 \|\phi_i^{n+1} - 2\phi_i^n + \phi_i^{n-1}\|^2 \geq 0. \quad \square \end{aligned} \tag{3.67}$$

**Remark 3.6.** It is worth noting that both IEQ and SAV (cf. [7,8,31,34–41]) use the same idea of “quadratzation”, and they are both effective to generate linear schemes for gradient flow type models. By using the inverse linear operator technique, SAV method can usually produce equations with constant coefficients thus it is more effective in practice. However, for the gradient flow model coupled with the hydrodynamics, it is quite difficult to apply the inverse linear operator due to the coupling nature between the phase-field variable and the velocity field. Recently, the author has developed the so-called “zero-energy-contribution” technique which can be combined with IEQ/SAV approach such that for hydrodynamics-coupled gradient flow systems, the fully-decoupled type scheme can be easily obtained, and all coupled, nonlocal calculations or variable-coefficient systems can be easily avoided, see [34–41].

#### 4. Numerical simulation

In this section, we perform numerical simulations in two and three-dimensional spaces to demonstrate the accuracy and energy stability of the developed scheme (3.14)–(3.22). Since the developed scheme has variable coefficients, so we use a conjugate gradient type solver with preconditioning (PCG), that does not need explicitly building the matrix. Instead, it only

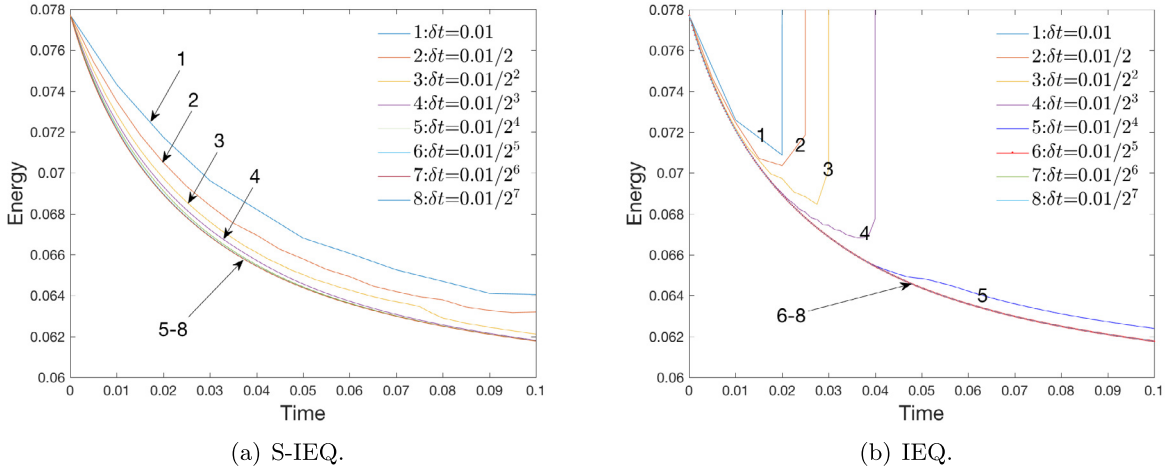


**Fig. 4.2.** The comparisons of the time evolution of the total free energy (3.51) with various time steps computed by using the scheme S-IEQ and IEQ, where we set the surface tension parameter as  $(\sigma_{12}, \sigma_{13}, \sigma_{23}) = 0.02(1, 1, 1)$ .

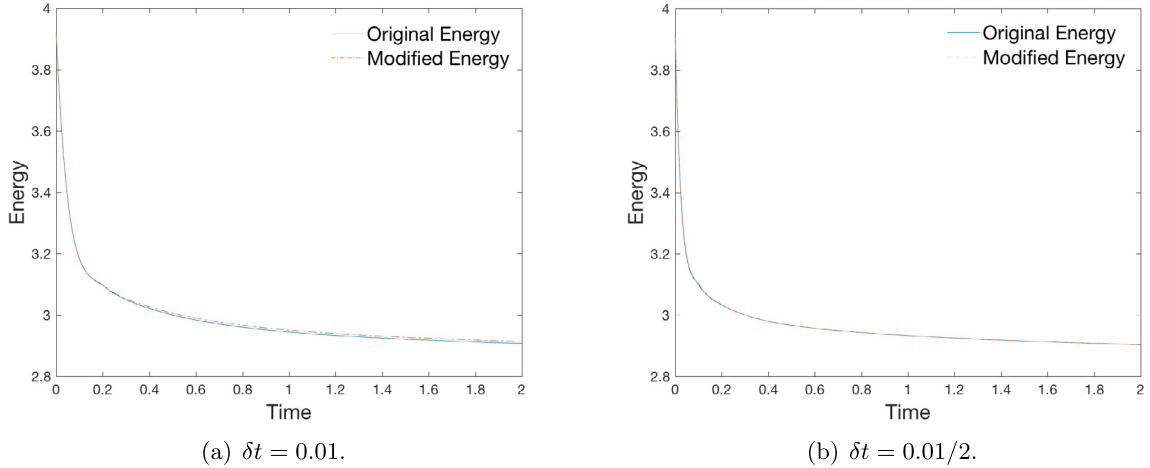


**Fig. 4.3.** The comparisons of the time evolution of the total free energy in the original form (2.13) and modified discrete form (3.51) with various  $\delta t$  computed by using the scheme S-IEQ, where we set the surface tension parameter as  $(\sigma_{12}, \sigma_{13}, \sigma_{23}) = 0.02(1, 1, 3)$ .

needs a subroutine to calculate the matrix-vector product. Since the linear systems are not symmetric, we use BiCGSTAB method.

#### 4.1. Accuracy and stability test

We first perform convergence and stability tests for the developed scheme (3.14)-(3.22). When the scheme is equipped with a non-zero stabilizer ( $S \neq 0$ ), we denote it by S-IEQ for short. In order to show how the stability is improved by the stabilization term, for comparisons, the convergence rates of the non-stabilized version are also calculated, namely, the scheme (3.14)-(3.22) without the stabilizer ( $S = 0$ ), denoted by IEQ for short.

We first perform refinement tests in time to investigate the temporal convergence rates. The 2D computational domain is set as  $\Omega = [0, 2] \times [0, 1]$ . The periodic boundary conditions are used for the  $x$ -axis which is discretized by the Fourier-spectral method. The boundary conditions (3.19) and (3.22) are used for the  $y$ -axis which is then discretized by using the Legendre-Galerkin method. The  $x$ -direction is calculated by using 257 Fourier modes, and the  $y$ -direction is calculated by using Legendre polynomials up to the degree of 256. Using this sufficient fine grid, the interface can be well resolved, so that the spatial errors are negligible compared with the temporal errors.

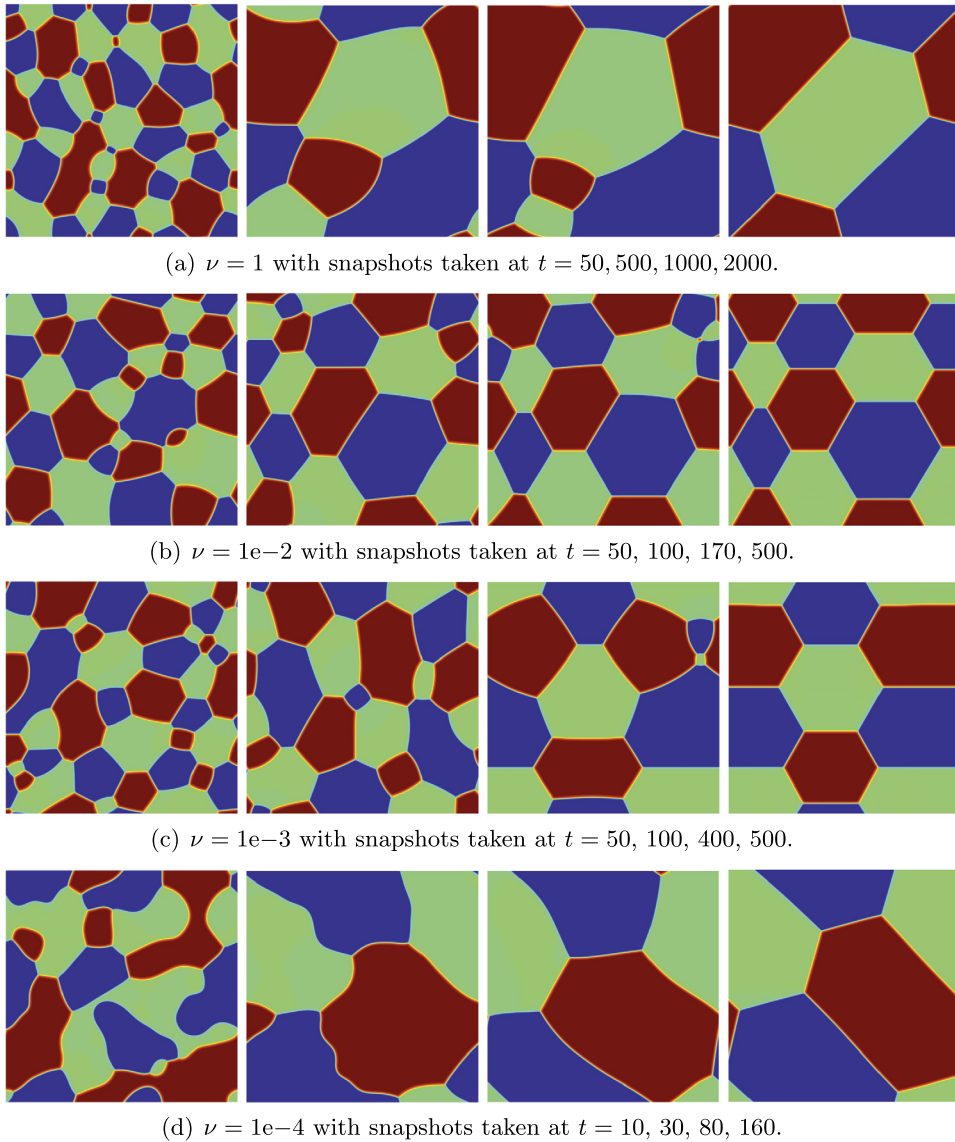


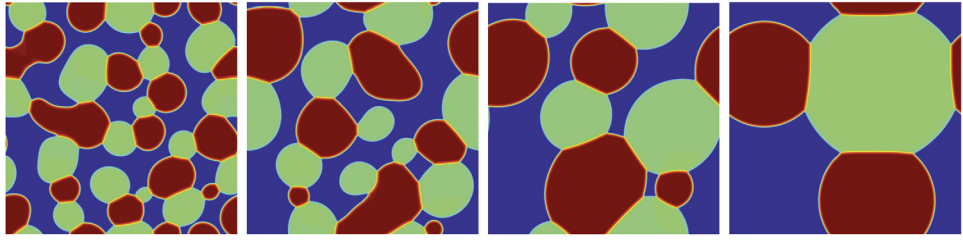
**Fig. 4.4.** The 2D dynamical evolution of the profile  $\frac{1}{2}\phi_1 + \phi_2$  for the spinodal decomposition examples with  $(\sigma_{12}, \sigma_{13}, \sigma_{23}) = 0.02(1, 1, 1)$  and various viscosity parameters  $\nu = 1, 1e-2, 1e-3,$  and  $1e-4$  are used.

The initial conditions are set as follows,

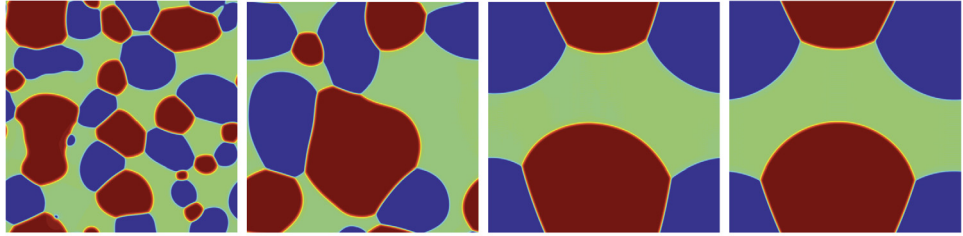
$$\begin{cases} \phi_i^0(x, y) = \tanh\left(\frac{r - \sqrt{(x - x_i)^2 + (y - y_i)^2}}{\epsilon}\right), i = 1, 2, \\ \phi_3^0(x, y) = 1 - \phi_1^0(x, y) - \phi_2^0(x, y), \\ \mathbf{u}^0(x, y) = \mathbf{0}, p^0(x, y) = 0, \end{cases} \quad (4.1)$$

where  $r = 0.25, x_1 = 1.27, x_2 = 0.73, y_1 = y_2 = 0.5$ . We set  $\nu = 1, \epsilon = 0.04, M = 2.5e-3, B = 10,$  and  $S = 10$ . Since the exact solution is not known, we choose the solution obtained with the time step size  $\delta t = 1e-9$  computed by the scheme S-IEQ as the benchmark solution (approximately the exact solution) for computing errors. We investigate the order of accuracy by using two different set of surface tension parameters  $(\sigma_{12}, \sigma_{23}, \sigma_{13})$ . The average of the  $L^2$  errors of the three phase-field variables, the average of the  $L^2$  errors of the velocity field, as well as the pressure between the numerical solution and the exact solution at  $t = 0.2$  are then plotted by varying the time step sizes.

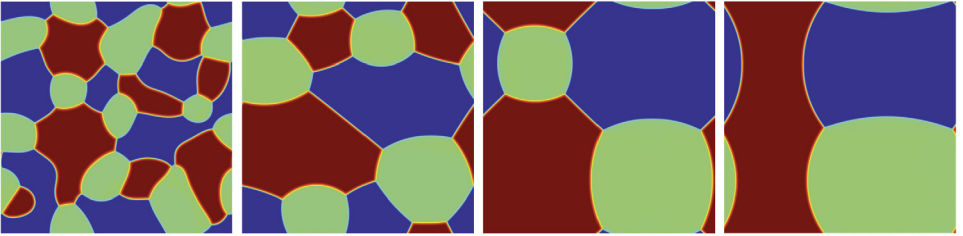
In Fig. 4.1 (a), for  $(\sigma_{12}, \sigma_{23}, \sigma_{13}) = 0.02(1, 1, 1)$ , we show the  $L^2$ -errors of all the variables by varying the time step sizes from  $\delta t = 0.1$  to  $\delta t = \frac{0.01}{2^7}$  with a factor of  $1/2$ . We observe that both of the two schemes, S-IEQ and IEQ, present the second-order convergence rate but the slope of the accuracy curve of the non-stabilized version is not ideally straight when the time step is large. This implies the accuracy of the non-stabilized version is not as good as the stabilized version



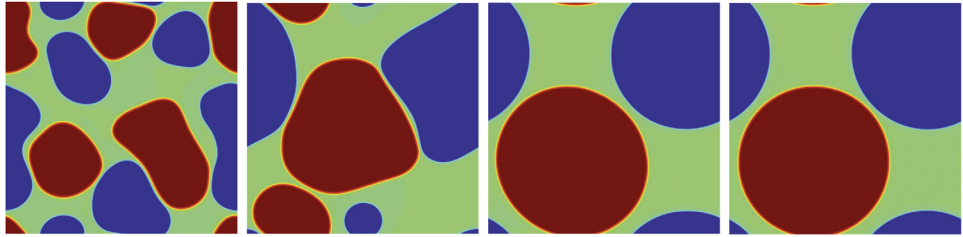
(a)  $(\sigma_{12}, \sigma_{13}, \sigma_{23}) = 0.02(1, 0.6, 0.6)$ ,  $\nu = 1e-3$  with snapshots taken at  $t = 10, 30, 100, 4000$ .



(b)  $(\sigma_{12}, \sigma_{13}, \sigma_{23}) = 0.02(1, 0.8, 1.4)$ ,  $\nu = 1e-3$  with snapshots taken at  $t = 10, 30, 100, 300$ .



(c)  $(\sigma_{12}, \sigma_{13}, \sigma_{23}) = 0.02(1, 1, 0.6)$ ,  $\nu = 1e-3$  with snapshots taken at  $t = 10, 100, 2000, 400$ .

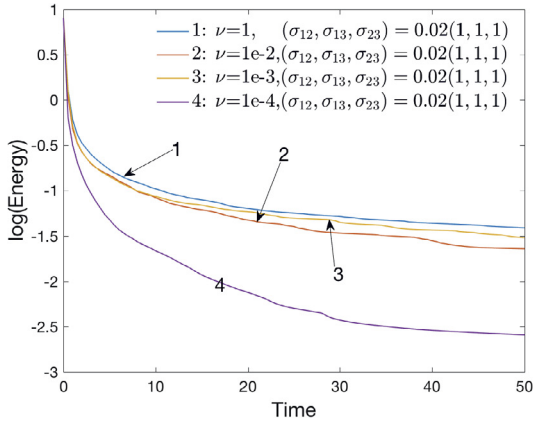


(d)  $(\sigma_{12}, \sigma_{13}, \sigma_{23}) = 0.02(1, 1, 3)$ ,  $\nu = 1e-3$  with snapshots taken at  $t = 10, 30, 100, 200$ .

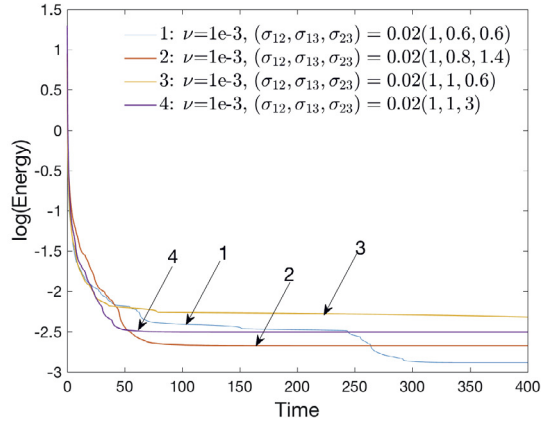
**Fig. 4.5.** The 2D dynamical evolution of the profile  $\frac{1}{2}\phi_1 + \phi_2$  for the spinodal decomposition example with  $\nu = 1e-3$  and four different sets of surface tension parameters  $(\sigma_{12}, \sigma_{13}, \sigma_{23})$ .

while using the large time steps. In Fig. 4.1 (b), we set  $(\sigma_{12}, \sigma_{23}, \sigma_{13}) = 0.02(1, 1, 3)$ . We observe that the scheme S-IEQ still presents almost perfect second-order accuracy. But the non-stabilized scheme IEQ presents zero-order convergence rate when  $\frac{0.01}{2^5} \leq \delta t \leq \frac{0.01}{2}$  or even blows up when  $\delta t = 0.01$ . It only presents the second-order accuracy when time step is very small ( $\delta t \leq 0.01/2^7$ ). In Fig. 4.1 (c), we set  $(\sigma_{12}, \sigma_{23}, \sigma_{13}) = 0.02(1, 0.6, 0.6)$  and compare the accuracy of S-IEQ and the second-order implicit-explicit type scheme (i.e., all linear terms are treated implicitly and nonlinear terms are treated explicitly, abbreviated as Semi). We observe that, when the time step is large, the scheme Semi blows up quickly therefore the corresponding error points are missing, when the time step is small, the scheme Semi shows second-order convergence, but scheme S-IEQ is still better than it from the magnitude of error.

We further plot the evolution curves of the total free energy (3.2) with various time steps for the second example computed by the scheme S-IEQ and IEQ in Fig. 4.2. We find that all computed energy curves computed by the scheme S-IEQ show monotonic decays, which confirms the unconditional stability of the scheme. For comparison, in Fig. 4.2(b), we plot the energy evolution curves calculated by using the non-stabilized scheme IEQ. The scheme IEQ blows up for larger time steps and only shows decays when  $\delta t \leq 0.16/2^4$ . In Fig. 4.3, we show the time evolution of the original energy (2.13) and

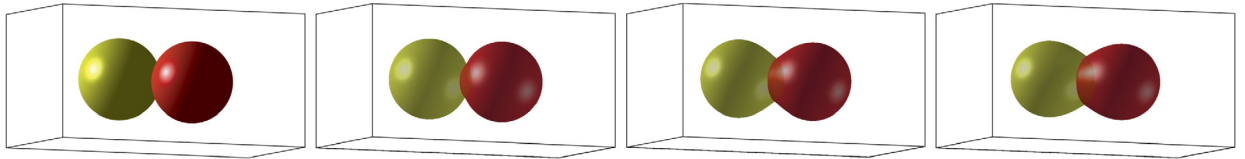


(a) Energy evolution with various  $\nu$ .

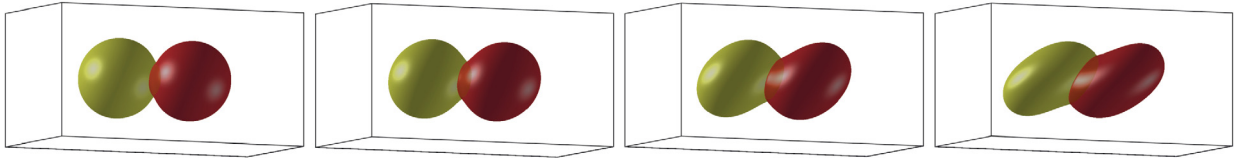


(b) Energy evolution with various  $(\sigma_{12}, \sigma_{13}, \sigma_{23})$ .

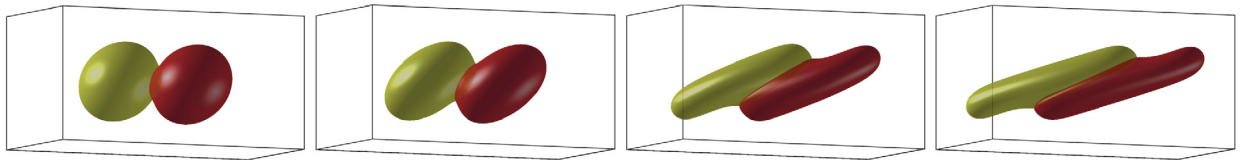
**Fig. 4.6.** Time evolution of the logarithm of the total free energy (3.2) for the spinodal decomposition examples where (a) the viscosity parameter is varied as  $\nu = 1, 1e-2, 1e-3, 1e-4$  and the surface tension parameter is fixed as  $(\sigma_{12}, \sigma_{13}, \sigma_{23}) = 0.02(1, 1, 1)$ , and (b) the surface tension parameters are varied as  $(\sigma_{12}, \sigma_{13}, \sigma_{23}) = 0.02(1, 0.6, 0.6), 0.02(1, 0.8, 1.4), 0.02(1, 1, 0.6)$ , and  $0.02(1, 1, 3)$  and the viscosity parameter is fixed as  $\nu = 1e-3$ .



(a) No shear case with  $\hat{u}_0 = 0$  where snapshots are taken at  $t = 0, 0.1, 1,$  and  $2.3$ .



(b) Weak shear case with  $\hat{u}_0 = 0.1$  where snapshots are taken at  $t = 0.1, 0.3, 1,$  and  $2.3$ .



(c) Strong shear case with  $\hat{u}_0 = 0.5$  where snapshots are taken at  $t = 0.1, 0.3, 1,$  and  $1.4$ .

**Fig. 4.7.** The 3D dynamical evolution of the two close-by spheres with the partial spreading case with  $(\sigma_{12}, \sigma_{13}, \sigma_{23}) = 0.02(1, 1, 1)$  that is driven by three different magnitude of shear flow where (a) no shear case with  $\hat{u}_0 = 0$ , (b) weak shear case with  $\hat{u}_0 = 0.1$ , and (c) strong shear case with  $\hat{u}_0 = 0.5$ .

modified energy (3.51) computed by using different time step size  $\delta t$ . When  $\delta t = 0.01$ , we can see the two energies have slight difference, but when  $\delta t = 0.01/2$ , there is no visible difference between them.

Finally, after summarizing all above accuracy and stability tests, we conclude that the stabilized scheme S-IEQ is far more superior to the non-stabilized scheme while using large time steps for both of the accuracy and the stability concern.

#### 4.2. Spinodal decomposition with various viscosity and surface tension parameters

In this example, we study how the viscosity of the fluid mixture and surface tension parameters affect the phase separation (or called spinodal decomposition) dynamics and equilibrium pattern. Using the homogeneous ternary mixture as the initial condition, we observe that the system evolves from the homogeneous to the three-phase state. The initial conditions read as follows,

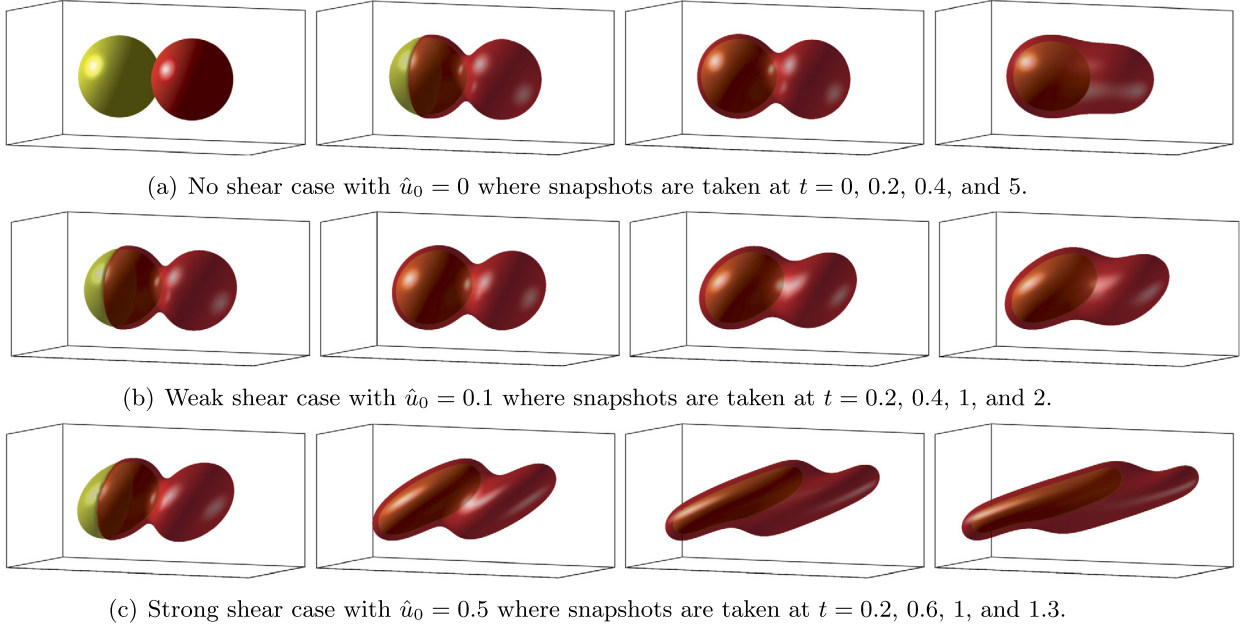


**Fig. 4.8.** The 3D dynamical evolution of the two close-by spheres with the total spreading case with  $(\sigma_{12}, \sigma_{13}, \sigma_{23}) = 0.02(1, 1, 3)$  that is driven by three different magnitude of shear flow where (a) no shear case with  $\hat{u}_0 = 0$ , (b) weak shear case with  $\hat{u}_0 = 0.1$ , and (c) strong shear case with  $\hat{u}_0 = 0.5$ .

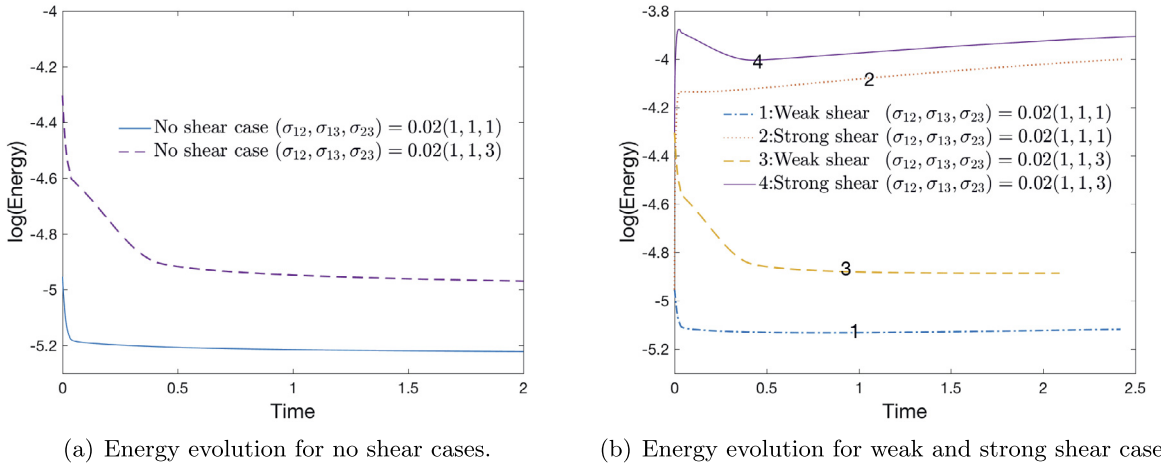


**Fig. 4.9.** Time evolution of the logarithm of the total free energy (3.2) for the two close-by spheres example with (a) no shear cases and (b) weak and strong shear cases where two sets of surface tension parameters are used,  $(\sigma_{12}, \sigma_{13}, \sigma_{23}) = 0.02(1, 1, 1)$  (partial spreading) and  $0.02(1, 1, 3)$  (total spreading). (Note: the total free energy is not decaying with time due to the imposed shear flow.)

$$\begin{cases} \mathbf{u}^0(\mathbf{x}) = \mathbf{0}, p^0(\mathbf{x}) = 0, \\ \psi_i(\mathbf{x}) = 0.5 + 0.001\text{rand}(\mathbf{x}), \\ \phi_i^0(\mathbf{x}) = \frac{\psi_i}{\psi_1 + \psi_2 + \psi_3}, i = 1, 2, 3, \end{cases} \quad (4.2)$$

where the  $\text{rand}(\mathbf{x})$  is the random number in  $[-1, 1]$  that follows the normal distribution.

We use the 2D computational domain  $[0, 2]^2$  and adopt the periodic boundary conditions. The space is discretized by using the Fourier-spectral methods with  $N_x = N_y = 257$  Fourier modes. The model parameters read as  $\delta t = 1e-3$ ,  $\epsilon = 0.02$ ,  $B = 10$ ,  $S = 20$ , and  $M = 5e-3$ . We adjust the viscosity parameter  $\nu$  and surface tensions  $(\sigma_{12}, \sigma_{13}, \sigma_{23})$  to investigate how the three phases are separated.

In Fig. 4.4, we perform simulations for a partial spreading case with three equal surface tension parameters  $(\sigma_{12}, \sigma_{13}, \sigma_{23}) = 0.02(1, 1, 1)$  and vary the viscosity parameter as  $\nu = 1, 1e-2, 1e-3,$  and  $1e-4$ . We observe the phase separation behavior and all the final equilibrium solutions present hexagonal patterns where the three contact angles become  $\frac{2\pi}{3}$ . Meanwhile, we find that the final equilibrium state is obtained faster while using smaller viscosity parameter.

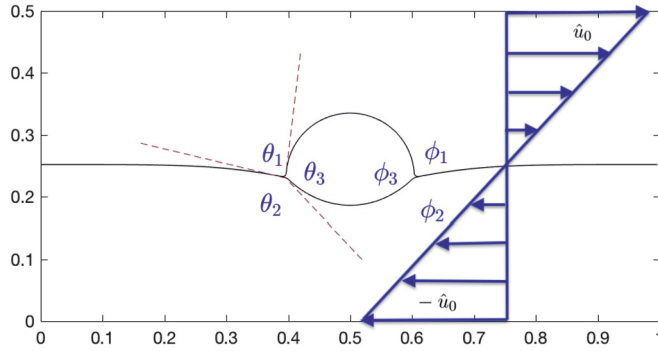


Fig. 4.10. Theoretical shape of the contact lens at the equilibrium between two stratified fluid components.

In Fig. 4.5, we fix  $\nu = 1e-3$  and vary the surface tension parameters to be  $(\sigma_{12}, \sigma_{13}, \sigma_{23}) = 0.02(1, 0.6, 0.6), 0.02(1, 0.8, 1.4), 0.02(1, 1, 0.6),$  and  $0.02(1, 1, 3),$  respectively. We then observe that the final equilibrium solution presents various contact angles. In particular, when  $(\sigma_{12}, \sigma_{13}, \sigma_{23}) = 0.02(1, 1, 3)$  shown in Fig. 4.5 (d), we observe that no junction points are formed all along due to the total spreading happens therein.

In Fig. 4.6, we present the time evolution of the free energy functional for all eight simulations. The energy curves show the decay with the time that confirms that the developed algorithm is unconditionally stable.

#### 4.3. Two close-by spheres under the shear flow

In this example, we perform simulations to investigate how the two close-by spheres are driven by the imposed shear flow on the boundary and the surface tension forces in 3D space. The computational domain is set as  $(x, y, z) \in \Omega = [0, 1] \times [0, 0.5] \times [0, 0.5].$

The initial conditions read as

$$\begin{cases} \mathbf{u}^0(\mathbf{x}) = \mathbf{0}, p^0(\mathbf{x}) = 0, \\ \phi_i^0(\mathbf{x}) = \frac{1}{2} \tanh\left(\frac{r_i - \sqrt{(x-x_i)^2 + (y-y_i)^2 + (z-z_i)^2}}{\epsilon}\right) + \frac{1}{2}, i = 1, 2, \\ \phi_3^0(\mathbf{x}) = 1 - \phi_1^0(\mathbf{x}) - \phi_2^0(\mathbf{x}), \end{cases} \quad (4.3)$$

where  $\epsilon = 0.018, r_1 = r_2 = 0.15, x_1 = 0.65, x_2 = 0.35,$  and  $y_1 = y_2 = z_1 = z_2 = 0.25.$  The periodic boundary conditions are set for the  $x-$  and  $y-$ directions which are discretized by using the Fourier-spectral method with  $129^2$  Fourier modes. The boundary conditions of the velocity field  $\mathbf{u} = (u, v, w),$  phase-field variables  $\phi_i,$  and the chemical potentials  $\mu_i$  along the  $z-$ direction are set as

$$u|_{(z=0,0.5)} = \pm \hat{u}_0, v|_{(z=0,0.5)} = w|_{(z=0,0.5)} = \partial_{\mathbf{n}}\phi_i|_{(z=0,0.5)} = \partial_{\mathbf{n}}\mu_i|_{(z=0,0.5)} = 0. \quad (4.4)$$

The  $z-$ direction is then discretized by using the Legendre-Galerkin spectral method where the Legendre polynomials up to the degree of 256 are adopted. For better accuracy, we use the time step  $\delta t = 1e-3.$  The other model parameters are set as  $\nu = 1, M = 1e-4, \epsilon = 0.015, B = 10, S = 10.$  We vary the surface tension parameters  $(\sigma_{12}, \sigma_{13}, \sigma_{23})$  and adjust the magnitude of the shear flow  $\hat{u}_0$  to investigate how the two spheres are deformed when time evolves.

First, using the partial spreading case with  $(\sigma_{12}, \sigma_{13}, \sigma_{23}) = (1, 1, 1),$  we adjust the magnitude of the imposed shear case by setting  $\hat{u}_0 = 0$  (no shear),  $\hat{u}_0 = 0.1$  (weak shear), and  $\hat{u}_0 = 0.5$  (strong shear). For the no shear case, shown in Fig. 4.7 (a), we observe that the two spheres are finally bound together with identical shapes due to the equal surface tension force between each phase. For the weak shear and strong shear cases, shown in Fig. 4.7 (b) and (c), we observe that the two bounded spheres are deformed to form ellipsoids due to the shear flow and larger shear flow induces larger deformations.

Second, we investigate the total spreading case with  $(\sigma_{12}, \sigma_{13}, \sigma_{23}) = (1, 1, 3).$  For the no shear case that is shown in Fig. 4.8(a), we find that one sphere finally moves into the other one since the latter phase spreads out totally. Likewise, for the weak shear and strong shear cases, shown in Fig. 4.8 (b) and (c), the two spheres are deformed by the shear flow field while one phase is totally spreading out around the other. The time evolution of the free energy functional for all cases is presented in Fig. 4.9.

#### 4.4. Liquid lens between two stratified fluids under the shear flow

In this subsection, we compute the evolutions of the liquid lens with and without the shear flow where the lens is initially spherical and located at the interface between two other immiscible fluids, cf. [4–6,45,46]. The 2D computed domain is set as  $[0, 1] \times [0, 0.5]$  and the initial conditions read as follows,

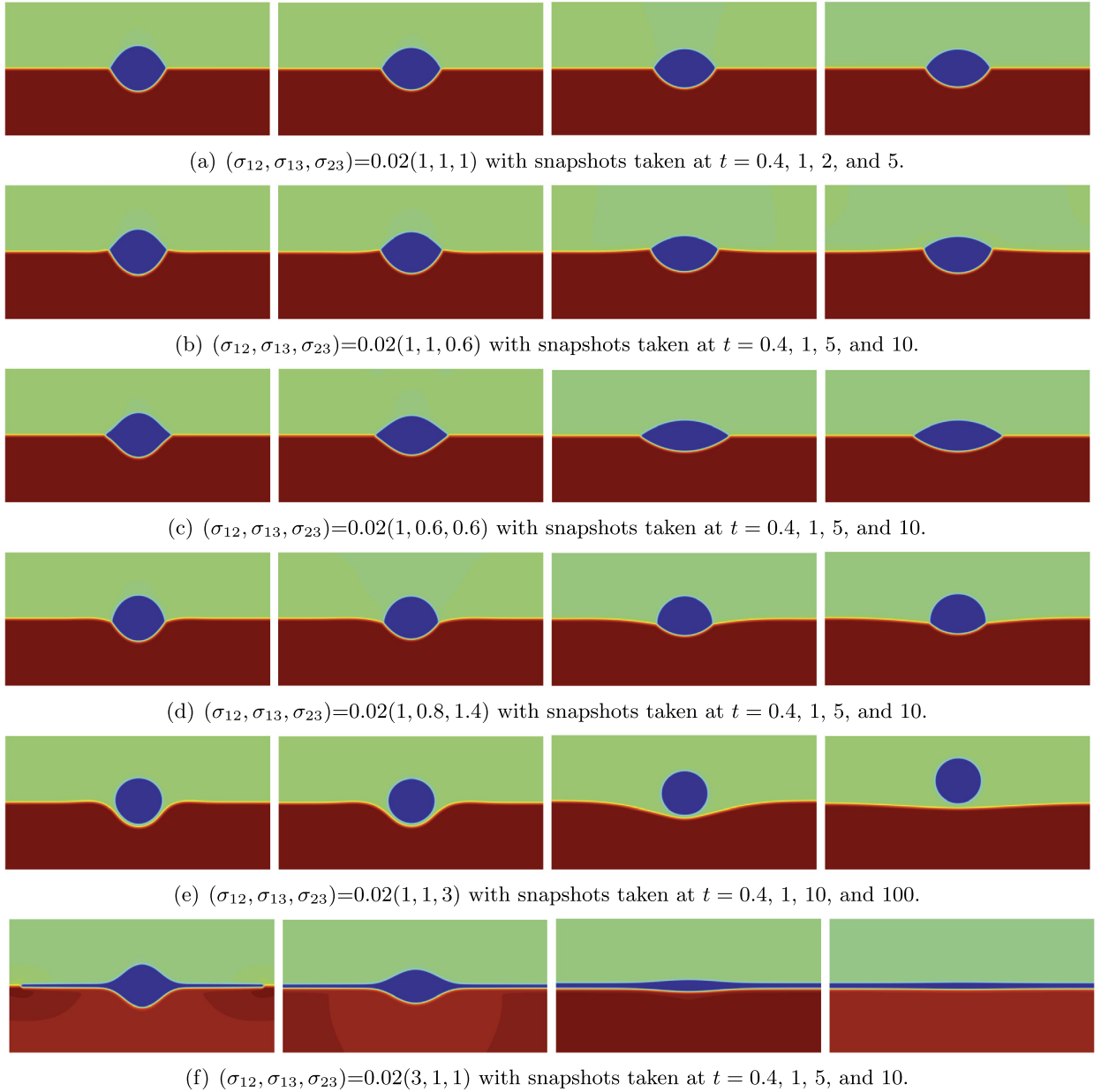
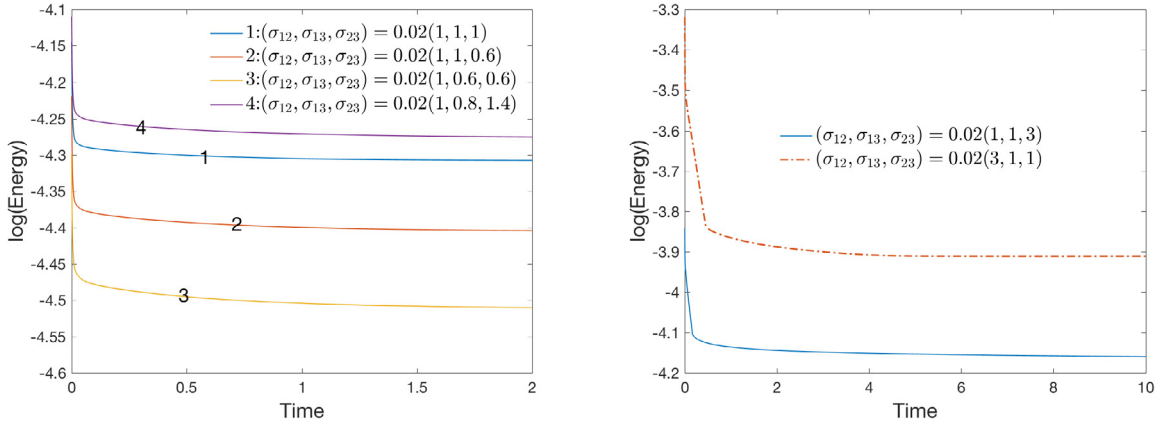


**Fig. 4.11.** The 2D dynamical evolution of the profile  $\frac{1}{2}\phi_1 + \phi_2$  for the liquid lens example without imposing the shear flow ( $\hat{u}_0 = 0$ ) where four partial spreading and two total spreading cases are simulated.

$$\begin{aligned}
 \mathbf{u}^0(x, y) &= \mathbf{0}, \quad p^0(x, y) = 0, \\
 \phi_1^0(x, y) &= (1 - \phi_3^0) \left( \frac{1}{2} + \frac{1}{2} \tanh\left(\frac{4}{\epsilon}(y - 0.25)\right) \right) \\
 \phi_2^0(x, y) &= 1 - \phi_1^0 - \phi_3^0, \\
 \phi_3^0(x, y) &= \frac{1}{2} \tanh\left(\frac{0.09 - \sqrt{(x - 0.5)^2 + (y - 0.25)^2}}{\epsilon/2}\right) + \frac{1}{2}.
 \end{aligned} \tag{4.5}$$

The periodic boundary conditions are set for the  $x$ -direction which is discretized by using the Fourier-spectral method with 257 Fourier modes. The boundary conditions for  $\mathbf{u} = (u, v)$ ,  $\phi_i$  and  $\mu_i$  along the  $y$ -direction are set as

$$u|_{(y=0,0.5)} = \pm \hat{u}_0, \quad v|_{(y=0,0.5)} = \partial_{\mathbf{n}} \phi_i|_{(y=0,0.5)} = \partial_{\mathbf{n}} \mu_i|_{(y=0,0.5)} = 0. \tag{4.6}$$



(a) Energy evolution for four partial spreading cases. (b) Energy evolution for two total spreading cases.

**Fig. 4.12.** (a) Time evolution of the logarithm of the total free energy (3.2) for the two close-by spheres example with (a) no shear cases and (b) weak and strong shear cases where  $(\sigma_{12}, \sigma_{13}, \sigma_{23}) = 0.02(1, 1, 1)$  and  $0.02(1, 1, 3)$ .

The  $y$ -direction is then discretized by using the Legendre-Galerkin spectral method with the Legendre polynomials up to the degree of 512. For better accuracy, we use the time step  $\delta t = 1e-3$ . We set the model parameters as  $\nu = 1$ ,  $M = 1e-4$ ,  $\epsilon = 0.01$ ,  $B = 10$ ,  $S = 10$ , and adjust the surface tension parameters  $(\sigma_{12}, \sigma_{13}, \sigma_{23})$  to investigate how the contact angles are affected.

As pointed by the Young's relation (cf. [6,19,27]), in the limit  $\epsilon \rightarrow 0$ , the contact angles (shown in Fig. 4.10) of the equilibrium state of the lens is given as a function of the three surface tensions by

$$\frac{\sin\theta_1}{\sigma_{23}} = \frac{\sin\theta_2}{\sigma_{13}} = \frac{\sin\theta_3}{\sigma_{12}}. \quad (4.7)$$

We first simulate four partial spreading cases ( $\Sigma_i > 0$ , for all  $i$ ) and two total spreading cases ( $\Sigma_i < 0$  for some  $i$ ) without imposing the shear flow (i.e.,  $\hat{u}_0 = 0$ ) in Fig. 4.11 where snapshots of the profile  $\frac{1}{2}\phi_1 + \phi_2$  at various times are plotted. From the sharp interface formula (4.7) for angles, we derive

- $\theta_1 = \theta_2 = \theta_3 = \frac{2\pi}{3}$  for  $(\sigma_{12}, \sigma_{13}, \sigma_{23}) = 0.02(1, 1, 1)$ ;
- $\theta_1 > \theta_2 = \theta_3$  for  $(\sigma_{12}, \sigma_{13}, \sigma_{23}) = 0.02(1, 1, 0.6)$ ;
- $\theta_1 = \theta_2 > \theta_3$  for  $(\sigma_{12}, \sigma_{13}, \sigma_{23}) = 0.02(1, 0.6, 0.6)$ ;
- $\theta_1 < \theta_3 < \theta_2$  for  $(\sigma_{12}, \sigma_{13}, \sigma_{23}) = 0.02(1, 0.8, 1.4)$ ;
- $\theta_1 = 0, \theta_2 = \theta_3 = \pi$  for  $(\sigma_{12}, \sigma_{13}, \sigma_{23}) = 0.02(1, 1, 3)$ ;
- $\theta_1 = \theta_2 = \pi, \theta_3 = 0$  for  $(\sigma_{12}, \sigma_{13}, \sigma_{23}) = 0.02(3, 1, 1)$ .

These theoretical predictions for contact angles are all verified by the computed results which are shown by the equilibrium solutions plotted in each final subfigure of Fig. 4.11 (a)-(f). Moreover, all these computations are qualitatively consistent to the numerical simulations presented in [4,6,43,45,46]. The time evolution of the free energy functional for all cases is presented in Fig. 4.12. Once we impose the shear flow on the boundary, all dynamical behaviors until the equilibrium states for each case are shown Fig. 4.13 (a)-(f). We observe that the flow field makes the total shape of the liquid lens deformed while the contact angles still follow the sharp interface formula (4.7).

#### 4.5. A compound droplet under the shear flow

In this example, we perform simulations to investigate how a compound droplet (drop-in-drop) are driven by the imposed shear flow on the boundary. The computational domain is set as  $(x, y) \in \Omega = [0, 1] \times [0, 0.75]$ .

The initial conditions read as

$$\begin{cases} \mathbf{u}^0(\mathbf{x}) = \mathbf{0}, p^0(\mathbf{x}) = 0, \\ \phi_1^0(\mathbf{x}) = -\frac{1}{2} \tanh\left(\frac{R_1 - \sqrt{(x-0.5)^2 + (y-0.35)^2}}{\epsilon}\right) + \frac{1}{2}, \\ \phi_3^0(\mathbf{x}) = \frac{1}{2} \tanh\left(\frac{R_2 - \sqrt{(x-0.5)^2 + (y-0.35)^2}}{\epsilon}\right) + \frac{1}{2}, \\ \phi_2^0(\mathbf{x}) = 1 - \phi_1^0(\mathbf{x}) - \phi_3^0(\mathbf{x}). \end{cases} \quad (4.8)$$

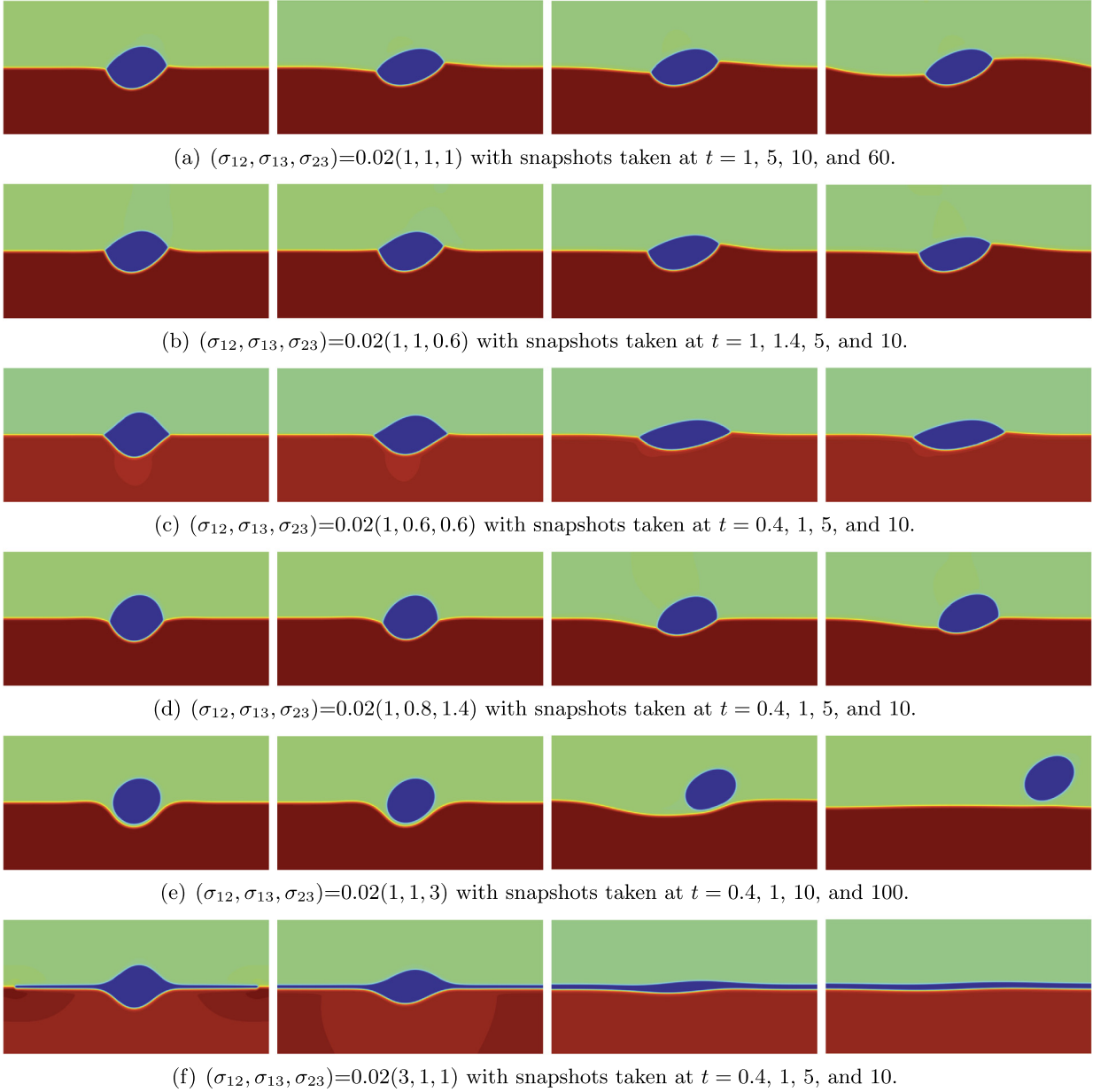


**Fig. 4.13.** The 2D dynamical evolution of the profile  $\frac{1}{2}\phi_1 + \phi_2$  for the liquid lens example with the shear flow ( $\hat{u}_0 = 0.1$ ) where four partial spreading and two total spreading cases are simulated.

The periodic boundary conditions are set for the  $x$ -direction which is discretized by using the Fourier-spectral method with 257 Fourier modes. The boundary conditions of the velocity field  $\mathbf{u} = (u, v)$ , phase-field variables  $\phi_i$ , and the chemical potentials  $\mu_i$  along the  $z$ -direction are set as

$$u|_{(z=0,0.75)} = \pm \hat{u}_0, \quad v|_{(z=0,0.75)} = \partial_{\mathbf{n}}\phi_i|_{(z=0,0.75)} = \partial_{\mathbf{n}}\mu_i|_{(z=0,0.75)} = 0. \quad (4.9)$$

The  $y$ -direction is then discretized by using the Legendre-Galerkin spectral method where the Legendre polynomials up to the degree of 512 are adopted. For better accuracy, we use the time step  $\delta t = 1e-3$ . The other model parameters are set as  $R_1 = 0.28$ ,  $\nu = 1$ ,  $M = 1e-4$ ,  $\epsilon = 0.01$ ,  $B = 10$ ,  $S = 10$ ,  $(\sigma_{12}, \sigma_{13}, \sigma_{23}) = (1, 0.6, 0.6)$ ,  $\hat{u}_0 = 1.2$ . We adjust the radius of the inner droplet  $R_2$  to investigate how the two drops are deformed when time evolves.

In Fig. 4.14, we plot the profiles of  $\frac{1}{2}\phi_1 + \phi_2$  of the steady-state solution, where the radius of inner droplet is set as  $R_2 = 0.1, 0.13, 0.16$ . We can see that with the different radius of the inner droplet, the deformation of the outer droplet is different. At the same time, the deformation of the smaller inner droplets is least affected by the shear flow, and the larger inner droplets are more affected. The inclination angles formed by the inner droplet and the outer droplet are completely

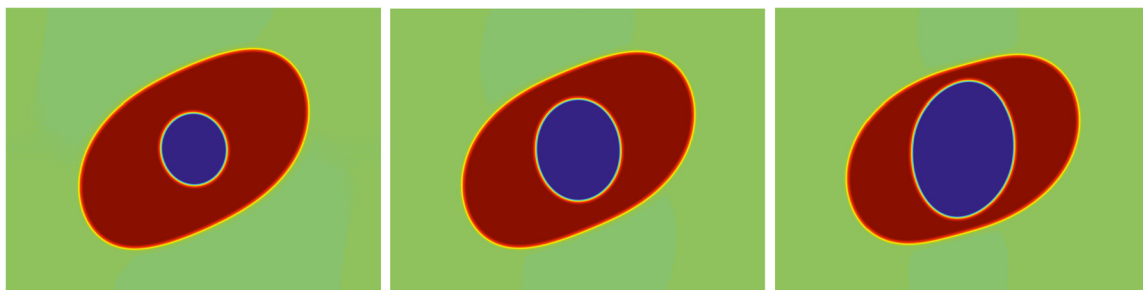


**Fig. 4.14.** The deformation of a compound droplet driven by the shear flow where the radius  $R_2$  of inner droplet is varied. From left to right,  $R_2 = 0.1, 0.13$  and  $0.16$ .

different. These simulations are qualitatively consistent with the numerical simulations in [16] using the immersed boundary method.

## 5. Concluding remarks

In this paper, we develop a semi-discrete in time, linear, and second-order scheme to solve the hydrodynamically coupled three components Cahn-Hilliard phase-field model. The scheme combines the recently developed IEQ approach with the stabilization technique, the projection method, as well as the implicit-explicit treatments for the nonlinear stress and convective terms. We prove the unconditional energy stability of the developed scheme rigorously. In simulating numerous numerical examples of 2D and 3D, we demonstrate the stability and the accuracy of the developed scheme numerically.

## CRedit authorship contribution statement

The author confirms sole responsibility for the following: algorithm development, data collection/production, analysis and interpretation of results, and manuscript preparation.

## Declaration of competing interest

The authors declare that they have no known competing financial interests or personal relationships that could have appeared to influence the work reported in this paper.

## Acknowledgements

X. Yang was partially supported by National Science Foundation with grant numbers DMS-1720212, DMS-1818783 and DMS-2012490.

## References

- [1] J.W. Barrett, J.F. Blowey, An improved error bound for a finite element approximation of a model for phase separation of a multi-component alloy, *IMA J. Numer. Anal.* 19 (1999) 147–168.
- [2] J.W. Barrett, J.F. Blowey, H. Garcke, On fully practical finite element approximations of degenerate Cahn-Hilliard systems, *ESAIM: M2AN* (35) (2001) 713–748.
- [3] J.F. Blowey, M.I.M. Copetti, C.M. Elliott, Numerical analysis of a model for phase separation of a multi-component alloy, *IMA J. Numer. Anal.* 16 (1996) 111–139.
- [4] F. Boyer, C. Lapuerta, Study of a three component Cahn-Hilliard flow model, *ESAIM: Math. Model. Numer. Anal.* 40 (4) (2006) 653–687.
- [5] F. Boyer, C. Lapuerta, S. Minjeaud, B. Piar, M. Quintard, Cahn-Hilliard/Navier-Stokes model for the simulation of three-phase flows, *Transp. Porous Media* 82 (2010) 463–483.
- [6] F. Boyer, S. Minjeaud, Numerical schemes for a three component Cahn-Hilliard model, *ESAIM: Math. Model. Numer. Anal.* 45 (04) (2011) 697–738.
- [7] C. Chen, X. Yang, Efficient numerical scheme for a dendritic solidification phase field model with melt convection, *J. Comput. Phys.* 388 (2019) 41–62.
- [8] C. Chen, X. Yang, Fast, provably unconditionally energy stable, and second-order accurate algorithms for the anisotropic Cahn-Hilliard model, *Comput. Methods Appl. Mech. Eng.* 351 (2019) 35–59.
- [9] C.M. Elliott, H. Garcke, Diffusional phase transitions in multicomponent systems with a concentration dependent mobility matrix, *Physica D* 109 (1997) 242–256.
- [10] D.J. Eyre, Unconditionally gradient stable time marching the Cahn-Hilliard equation, in: *Computational and Mathematical Models of Microstructural Evolution*, San Francisco, CA, 1998, in: *Mater. Res. Soc. Sympos. Proc.*, vol. 529, MRS, 1998, pp. 39–46.
- [11] X. Feng, A. Prohl, Numerical analysis of the Allen-Cahn equation and approximation for mean curvature flows, *Numer. Math.* 94 (2003) 33–65.
- [12] Xiaobing Feng, Yinnian He, Chun Liu, Analysis of finite element approximations of a phase field model for two-phase fluids, *Math. Compet.* 76 (258) (2007) 539–571 (electronic).
- [13] H. Garcke, B. Nestler, B. Stoth, A multiphase field concept: numerical simulations of moving phase boundaries and multiple junctions, *SIAM J. Appl. Math.* 60 (2000) 295–315.
- [14] H. Garcke, B. Stinner, Second order phase field asymptotics for multi-component systems, *Interfaces Free Bound.* 8 (2006) 131–157.

- [15] M.E. Gurtin, D. Polignone, J. Viñals, Two-phase binary fluids and immiscible fluids described by an order parameter, *Math. Models Methods Appl. Sci.* 6 (6) (1996) 815–831.
- [16] H. Hua, J. Shin, J. Kim, Dynamics of a compound droplet in shear flow, *Int. J. Heat Fluid Flow* 50 (2014) 63–71.
- [17] J. Kim, Phase-field models for multi-component fluid flows, *Commun. Comput. Phys.* 12 (3) (2012) 613–661.
- [18] J. Kim, K. Kang, J. Lowengrub, Conservative multigrid methods for ternary Cahn-Hilliard systems, *Commun. Math. Sci.* 2 (2004) 53–77.
- [19] J. Kim, J. Lowengrub, Phase field modeling and simulation of three-phase flows, *Interfaces Free Bound.* 7 (2005) 435–466.
- [20] H.G. Lee, J. Kim, A second-order accurate non-linear difference scheme for the n-component Cahn-Hilliard system, *Physica A* 387 (2008) 4787–4799.
- [21] C. Liu, J. Shen, X. Yang, Decoupled energy stable schemes for a phase-field model of two-phase incompressible flows with variable density, *J. Sci. Comput.* 62 (2015) 601–622.
- [22] J. Lowengrub, A. Ratz, A. Voigt, Phase field modeling of the dynamics of multicomponent vesicles spinodal decomposition coarsening budding and fission, *Phys. Rev. E* 79 (3) (2009).
- [23] L. Ma, R. Chen, X. Yang, H. Zhang, Numerical approximations for Allen-Cahn type phase field model of two-phase incompressible fluids with moving contact lines, *Commun. Comput. Phys.* 21 (2017) 867–889.
- [24] C. Miehe, M. Hofacker, F. Welschinger, A phase field model for rate-independent crack propagation: robust algorithmic implementation based on operator splits, *Comput. Methods Appl. Mech. Eng.* 199 (2010) 2765–2778.
- [25] S. Minjeaud, An unconditionally stable uncoupled scheme for a triphasic Cahn-Hilliard/Navier-Stokes model, *Numer. Methods Partial Differ. Equ.* 29 (2013) 584–618.
- [26] B. Nestler, H. Garcke, B. Stinner, Multicomponent alloy solidification: phase-field modeling and simulations, *Phys. Rev. E* 71 (2005) 041609.
- [27] J.S. Rowlinson, B. Widom, *Molecular Theory of Capillarity*, Clarendon Press, Oxford, 1989.
- [28] J. Shen, X. Yang, Numerical approximations of Allen-Cahn and Cahn-Hilliard equations, *Discrete Contin. Dyn. Syst.* 28 (2010) 1669–1691.
- [29] J. Shen, X. Yang, Decoupled energy stable schemes for phase field models of two phase complex fluids, *SIAM J. Sci. Comput.* 36 (2014) B122–B145.
- [30] J. Shen, X. Yang, Decoupled, energy stable schemes for phase-field models of two-phase incompressible flows, *SIAM J. Numer. Anal.* 53 (1) (2015) 279–296.
- [31] J. Shen, X. Yang, The IEQ and SAV approaches and their extensions for a class of highly nonlinear gradient flow systems, *Contemp. Math.* 754 (2020) 217–245.
- [32] J. Shen, X. Yang, H. Yu, Efficient energy stable numerical schemes for a phase field moving contact line model, *J. Comput. Phys.* 284 (2015) 617–630.
- [33] J. van Kan, A second-order accurate pressure-correction scheme for viscous incompressible flow, *SIAM J. Sci. Stat. Comput.* 7 (3) (1986) 870–891.
- [34] X. Yang, A new efficient fully-decoupled and second-order time-accurate scheme for Cahn-Hilliard phase-field model of three-phase incompressible flow, *Comput. Methods Appl. Mech. Eng.* 376 (2021) 13589.
- [35] X. Yang, A novel fully-decoupled scheme with second-order time accuracy and unconditional energy stability for the Navier-Stokes equations coupled with mass-conserved Allen-Cahn phase-field model of two-phase incompressible flow, *Int. J. Numer. Methods Eng.* 122 (2021) 1283–1306.
- [36] X. Yang, A novel fully-decoupled, second-order and energy stable numerical scheme of the conserved Allen-Cahn type flow-coupled binary surfactant model, *Comput. Methods Appl. Mech. Eng.* 373 (2021) 113502.
- [37] X. Yang, A novel fully-decoupled, second-order time-accurate, unconditionally energy stable scheme for a flow-coupled volume-conserved phase-field elastic bending energy model, *J. Comput. Phys.* 432 (2021) 110015.
- [38] X. Yang, A novel second-order time marching scheme for the Navier-Stokes/Darcy coupled with mass-conserved Allen-Cahn phase-field models of two-phase incompressible flow, *Comput. Methods Appl. Mech. Eng.* 377 (2021) 113597.
- [39] X. Yang, Numerical approximations of the Navier-Stokes equation coupled with volume-conserved multi-phase-field vesicles system: fully-decoupled, linear, unconditionally energy stable and second-order time-accurate numerical scheme, *Comput. Methods Appl. Mech. Eng.* 375 (2021) 113600.
- [40] X. Yang, On a novel fully-decoupled, linear and second-order accurate numerical scheme for the Cahn-Hilliard-Darcy system of two-phase Hele-Shaw flow, *Comput. Phys. Commun.* 263 (2021) 107868.
- [41] X. Yang, On a novel fully-decoupled, second-order accurate energy stable numerical scheme for a binary fluid-surfactant phase-field model, *SIAM J. Sci. Comput.* 43 (2021) B479–B507.
- [42] X. Yang, J.J. Feng, C. Liu, J. Shen, Numerical simulations of jet pinching-off and drop formation using an energetic variational phase-field method, *J. Comput. Phys.* 218 (2006) 417–428.
- [43] X. Yang, J. Zhao, Q. Wang, J. Shen, Numerical approximations for a three components Cahn-Hilliard phase-field model based on the invariant energy quadratization method, *Math. Models Methods Appl. Sci.* 27 (2017) 1993–2030.
- [44] H. Yu, X. Yang, Decoupled energy stable schemes for phase field model with contact lines and variable densities, *J. Comput. Phys.* 334 (2017) 665–686.
- [45] J. Zhang, X. Yang, Decoupled, non-iterative, and unconditionally energy stable large time stepping method for the three-phase Cahn-Hilliard phase-field model, *J. Comput. Phys.* 404 (2020) 109115.
- [46] J. Zhang, X. Yang, Unconditionally energy stable large time stepping method for the L2-gradient flow based ternary phase-field model with precise nonlocal volume conservation, *Comput. Methods Appl. Mech. Eng.* 361 (2020) 112743.